Genetic-Morphological Synergy Governs Cell Fate Specification in Development

Guoye Guan (关国业)[1,3,a,b], Yixuan Chen (陈宜煊)[2,3], Hongli Wang (王宏利)[1,2,4,*]

[1] Center for Quantitative Biology, Peking University, Beijing 100871, China

[2] State Key Laboratory for Artificial Microstructures and Mesoscopic Physics, School of Physics, Peking University, Beijing 100871, China

[3] These authors contributed equally.

[4] Lead Contact

[a] Present address: Department of Systems Biology, Harvard Medical School, Boston 02115, USA

[b] Present address: Department of Data Science, Dana-Farber Cancer Institute, Boston 02215, USA

[*] Correspondence: hlwang@pku.edu.cn (H.W.)

Cover Page

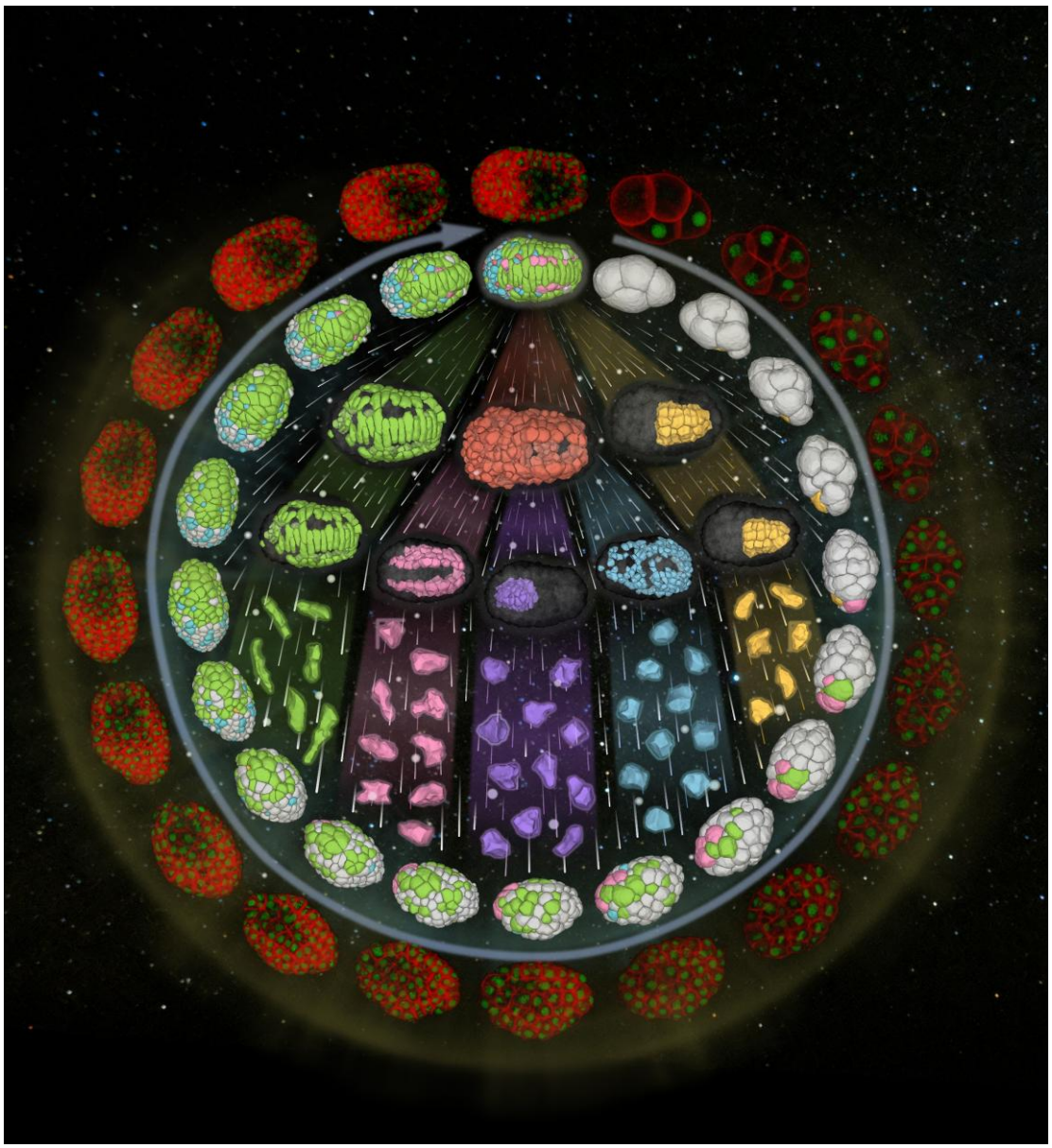

Cover Story

Cover Story: **Stellar orbits in the odyssey of embryonic development.**

The fluorescence (green/GFP: cell nucleus; red/mCherry: cell membrane; outer ring) and segmentation (utilizing both cell nucleus and cell membrane fluorescence; inner ring) snapshots of worm *Caenorhabditis elegans* embryos rotate clockwise like a celestial trajectory, chronicling embryonic development from 4-cell to 550-cell stages. Analogous to the primordial unfolding of galactic arms, morphological differentiation within an organism unfolds across hierarchical scales: from the early formation of germ layers (endoderm, mesoderm, and ectoderm) to the late emergence of tissues and organs (skin, muscle, pharynx, neurons, and intestine), ultimately down to each and every cell. As these stellar orbits expand, individual cells scatter like shooting stars, each carrying a differentiated morphology distinct to its specified fates. This journey through a morphodynamic cascade unveils the exquisitely encoded logic orchestrating life from gene expressions to cell morphologies in concert, culminating in the stereotyped spatiotemporal patterns of cell fate.

Graphical abstract

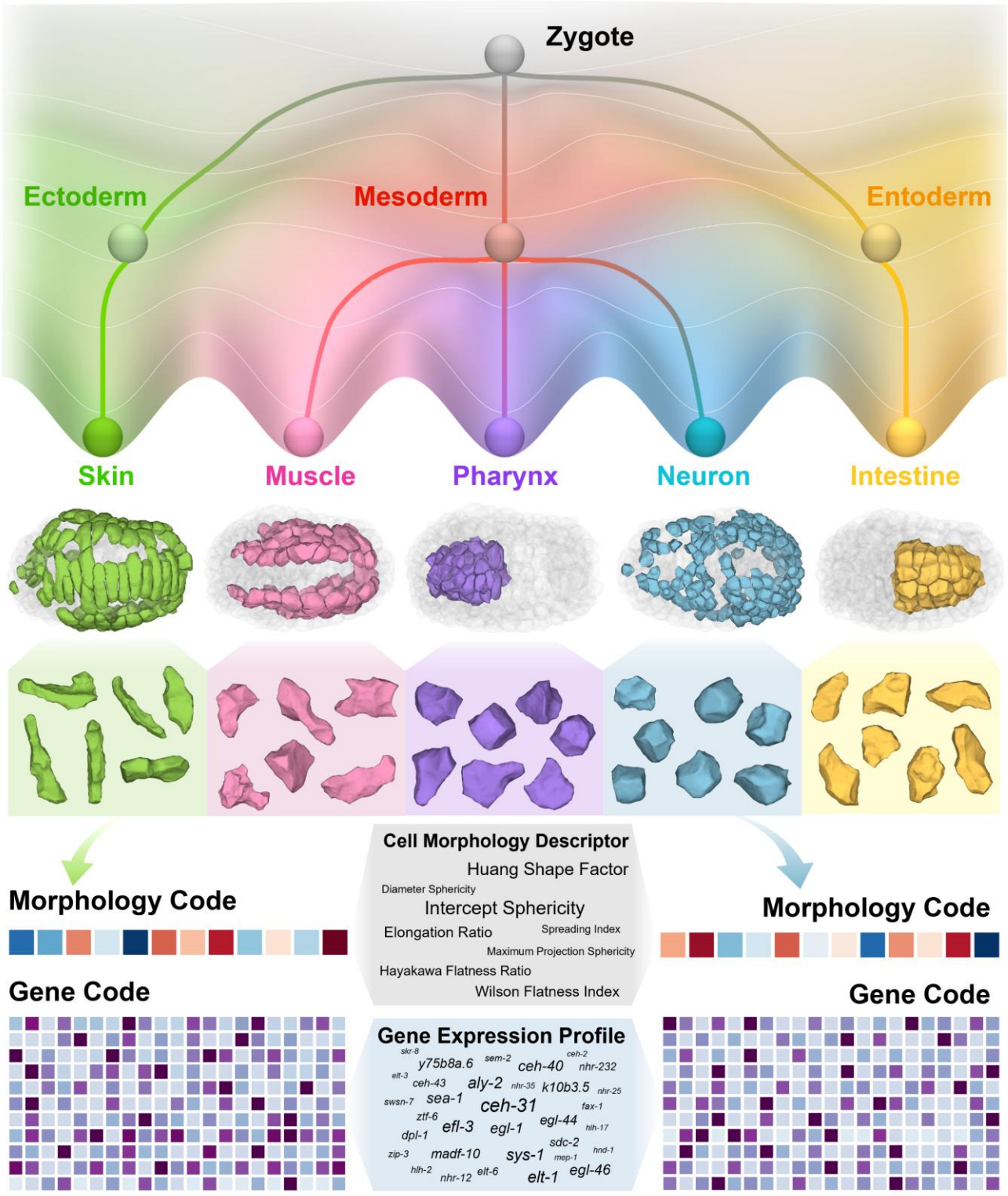

In brief

Cell fates are characterized by distinct features that uniquely identify each cell. Using 12 cell morphology descriptors and 412 gene expression profiles across lineage-resolved *C. elegans* embryos, Guan et al. demonstrate that cell fate specification proceeds through coupled or decoupled differentiation in gene expression and cell morphology, providing novel identifiers and resources for studying cell fate regulatory mechanisms in development. Cellular behaviors, encompassing asymmetric division, intercalating movement, and hierarchical differentiation from germ layers to specific cell types, are effectively

predictable.

Highlights

- 3D morphology descriptors can characterize various cellular states quantitatively.
- Developmental cell morphology accuracy is regulated and robust.
- Cell morphology and gene expression differentiations can be coupled or decoupled.
- Customized morphology descriptors sensitively distinguish cell fates across scales.

KEYWORDS

Cell morphology, gene expression, cell fate differentiation, differentiation, decoupling and coupling, metazoan development, germ layer, tissue and organ, body axis, *Caenorhabditis elegans* embryogenesis

SUMMARY

Cell morphology reflects cellular states, particularly cell fates with specific spatiotemporal features, like the spreading of epidermal cells in skin. However, how cell morphology relates to cell fate and genetic programs remains unclear. In this study, we leveraged the up-to-date lineage-resolved 3D cell morphology dataset of worm *Caenorhabditis elegans* embryogenesis. Twelve quantitative morphology descriptors reveal that cell morphology variation is tightly controlled and robust against mechanical compression, but not Notch signaling blocking. Integrating expression profiles of 412 genes, genetic and morphological differentiations between sister sublineages are identified in either coupled or decoupled manners, specifying cell fates from the formation of germ layers and tissues/organs to body axis establishment. Remarkably, customized morphology descriptors significantly distinguish cell fates (*e.g.*, neuron, pharynx, muscle, intestine, skin) with a few dozen 3D cell region samples. Together, these results uncover the genetic-morphological regulatory architectures during development synergistically and point toward medical and engineering applications with cell morphologies as novel biosensors.

INTRODUCTION

Cell morphology, defined by the three-dimensional (3D) geometry of the cell membrane boundary, is one of the most fundamental characteristics of a cell, reflecting its state, including division, movement, fate, and so forth [Dibus et al., *Curr. Opin. Cell Biol.*, 2024]. Of importance, it reflects the cell fate in conjunction with specific functional roles at cell- and tissue/organ- scales [Luxenburg et al., *Exp. Cell Res.*, 2019; Lim et al., *Nat. Rev. Mol. Cell Biol.*, 2021; Wu et al., *Annu. Rev. Cell Dev. Biol.*, 2023; Uriu et al., *Semin. Cell Dev. Biol.*, 2023]. For example, in human, elliptical adipocytes optimize lipid storage for energy reserves and organ protection [Cedikova et al., *Stem Cells Int.*, 2016]; immune cells extend pseudopodia to enable rapid chemotactic migration toward infection sites [Ridley et al., *Science*, 2003]. On the contrary, aberrant cell morphology could be indicative of pathological states, making morphological analysis a valuable

diagnostic tool [Alizadeh et al., *Comput. Biol. Med.*, 2020]. Automated image recognition approaches have been employed to detect early signs of cancer, inflammation, and infection. For example, variations in red blood cell morphology are indicative of different types of anemia [Lee et al., *Pattern Recogn. Lett.*, 2014; Bhaskar et al., *bioRxiv*, 2019], while irregularities in cancer cell morphology are indicative of different levels of invasive and metastatic potential [Friedl et al., *Nat. Rev. Mol. Cell Biol.*, 2009; Hanahan et al., *Cell*, 2011]. Although specific patterns of differential gene expression have been shown to underlie cell fate specification, whether concurrent differentiation in cell morphology represents a causal driver, a downstream consequence, or a parallel byproduct of cell fate determination remains an open and intriguing question.

Unlike gene expression, although cell morphology is known to reflect cell fate in many ways, it remains difficult to analyze in a systematic and quantitative manner. This difficulty arises because obtaining complete, high-quality 3D cell morphology datasets for entire developing samples demands exceptional spatiotemporal precision in both image acquisition and processing, yet is constrained by experimental (*e.g.*, phototoxicity and photobleaching) and computational limitations (*e.g.*, denoising and segmentation) [Guan et al., *Comput. Struct. Biotechnol. J.*, 2022]. As a result, most current studies examining cell morphology, gene expression, and their influence on cell fate specification focus on 2D datasets or 3D datasets encompassing only a limited number of cell fates [Benkeder et al., *eLife*, 2025; Ramezani et al., *Nat. Methods*, 2025; Tolonen et al., *bioRxiv*, 2025]. Recent breakthroughs in light imaging, combined with continuously optimized fluorescent reporters and cell membrane segmentation pipelines, now enable long-term time-lapse 3D imaging and reconstruction of hundreds to thousands of cells within developing samples [Leggio et al., *Nat. Commun.*, 2019]. Such image reconstruction has been conducted in a lot of species, including both animals (*e.g.*, worm [Azuma et al., *BMC Bioinformatics*, 2017], ascidian [Sladitschek et al., *Cell*, 2020], fly [Khan et al., *Development*, 2014], frog [Laznovsky et al., *Gigascience*, 2024], mouse [Xie et al., *Cell*, 2025], zebrafish [Stegmaier et al., *Dev. Cell*, 2016], human [Junyent et al., *Cell*, 2024]) and plants (*e.g.*, *Arabidopsis* [Truernit et al., *Plant Cell*, 2008], rice [Sato et al., *Int. J. Mol. Sci.*, 2021], *Nicotiana tabacum* [Pasternak et al., *Plant J.*, 2017]).

Among the species above, the roundworm/nematode *Caenorhabditis elegans* (*abbr.*, *C. elegans*) has served as a premier model for studying cell fate specification and morphogenesis over the past half-century, owing to its invariant cell lineage that produces all kinds of cell fates through precisely orchestrated spatiotemporal programs. [Sulston, *Philos. Trans. R. Soc. Lond. B Biol. Sci.*, 1976; Sulston et al., *Dev. Biol.*, 1977; Sulston et al., *Dev. Biol.*, 1983; Kaletta et al., *Nature*, 1997]. On one hand, its entire genome has been sequenced completely [*C. elegans* Sequencing Consortium, *Science*, 1998], and numerous genetic regulatory modules have been discovered [Brenner, *Genetics*, 1974; Green et al., *Cell*, 2024]. On the other hand, its transparent body permits non-invasive, low-damage live imaging throughout the entire embryogenesis, enabling the advance of automated 3D cell nucleus tracking [Bao et al., *Proc. Natl. Acad. Sci. U. S. A.*, 2006; Boyle et al., *BMC Bioinformatics*, 2006; Murray et al., *Nat. Protoc.*, 2006; Azuma et al., *Biomed. Eng. Lett.*, 2014], cell membrane segmentation [Azuma et al., *BMC Bioinformatics*, 2017;

Azuma et al., *Front. Bioinform.*, 2023; Xiong et al., *PLoS One*, 2020; Thiels et al., *Bioinformatics*, 2021], and gene expression profiling [Murray et al., *Nat. Methods*, 2008; Murray et al., *Genome Res.*, 2012; Hunt-Newbury et al., *PLoS Biol.*, 2007; Katzman et al., *BMC Bioinformatics*, 2018] with cell lineage resolved. These advances have culminated in the very recent reconstruction of comprehensive 3D cellular morphological maps throughout *C. elegans* embryogenesis, allowing integrative analyses across cell morphology, gene expression, cell fate, lineage, identity, division, position, and so forth [Guan et al., *Nat. Commun.*, 2025].

To figure out how cell fate specification interacts with morphogenesis during development, we devised a computational framework that integrates cell morphology descriptors with gene expression profiles to identify differentiation in each aspect upon cell division. Despite cell morphology descriptors are alternative depending on the chosen methods [Yu et al., *Adv. Healthc. Mater.*, 2013; Haupt et al., *J. Cell Sci.*, 2018; Chen et al., *Biomaterials*, 2016; van Bavel et al., *Bioinformatics*, 2023; Vadori et al., *arXiv*, 2024], here we firstly demonstrate that a set of 12 3D morphology descriptors quantitatively capture key cellular processes using *C. elegans* embryonic datasets [Cao et al., *Nat. Commun.*, 2020; Cao et al., *Quant. Biol.*, 2024; Guan et al., *Membranes*, 2024; Guan et al., *Nat. Commun.*, 2025], exemplified by asymmetric cell divisions and intercalation movements. These descriptors suggest that cell morphology is precisely regulated across individual embryos — such precision is robust against mechanical compression, yet becomes vulnerable when intercellular signaling is blocked, leading to harmful violation in cell-cell contact maps. Joint analyses of 12 cell morphology descriptors and 412 gene expression profiles further uncover distinct cell populations with coupling or decoupling between the two dimensions. Such coupling occurs at all levels of cell fate specification hierarchically, from germ layers to major somatic tissues/organs and their internal specific cell types along defined body axes. Together, our findings reveal a broad prevalence of co-differentiation between cell morphology and gene expression, establishing morphology as a powerful biosensor for distinguishing cell fates and providing an informative resource for systematically studying developmental regulation across dimensions.

RESULTS

3D cell morphology descriptors can characterize diverse cellular states quantitatively.

Morphology is known to reflect cellular states. For example, both dividing and intercalating cells undergo radial symmetry breaking with distinct morphological features denoting the formation of an axis [Jankele et al., *eLife*, 2021; Azuma et al., *Front. Bioinform.*, 2023; Khatri et al., *npj Syst. Biol. Appl.*, 2025; Walck-Shannon et al., *Nat. Rev. Mol. Cell Biol.*, 2014; Collinet et al., *Nat. Cell Biol.*, 2015; Heller et al., *Dev. Cell*, 2014]. Here, we test if a series of previously summarized 3D cell morphology descriptors (*incl.*, General Sphericity, Diameter Sphericity, Intercept Sphericity, Maximum Projection Sphericity, Hayakawa Roundness, Spreading Index, Elongation Ratio, Pivotability Index, Wilson Flatness Index, Hayakawa

Flatness Index, Huang Shape Factor, and Corey Shape Factor) can accurately characterize dynamic cellular states [Guan et al., *Membranes*, 2024] (Figure 1A). In brief, for a given 3D cell object, its volume, surface area, and those of its convex hull, along with the lengths of its three principal axes, are calculated. These intermediate parameters are then combined to derive 12 morphology descriptors with explicit geometric significance (Figure 1A). These descriptors have been successfully employed for quantitative feature extraction from biological cells, gravel particles, feldspar crystals, and glass shards [Wilson et al., *Earth Planet. Sci. Lett.*, 1979; Hayakawa et al., *Comput. Geosci.*, 2005; Yu et al., *Adv. Healthc. Mater.*, 2013]. To evaluate their capacity to characterize dynamic cellular states, we take the dividing cells and intercalating cells during *C. elegans* embryogenesis as representative examples (Table S1) [Guan et al., *Nat. Commun.*, 2025].

In theory, both dividing and intercalating cells can exhibit leveled morphological features associated with their behaviors (Figure 1B-1D). For dividing cells, the higher the volume asymmetry between daughter cells, the more unequal the cell morphology's two poles become (mathematically modellable as two overlapping spheres of unequal size); for intercalating cells, the more ingressing the cell is, the more squeezed the cell morphology becomes (mathematically modellable with a sphere bisected by a cylindrical intrusion) (Figure 1D; METHOD DETAILS). First of all, given a mathematically modeled 3D cell object with varying division or intercalation levels (division asymmetry and intercalation depth over time), the theoretical values of these morphology descriptors can be accurately computed numerically, demonstrating their feasibility for application to voxel-based data in practice (Figure S1A-S1C). Mathematical analysis further revealed clear correlations between specific morphology descriptors and the levels of division asymmetry or intercalation depth — for example, Elongation Ratio showed the strongest correlation with division asymmetry and General Sphericity with intercalation depth (Figure 1E and 1F); these theoretical relationships were consistently recapitulated by empirical data from *C. elegans* embryos (Figure 1E and 1F; Figure S1D; METHOD DETAILS).

Furthermore, since cell division [Rose et al., *WormBook*, 2014] and intercalation [Walck-Shannon et al., *Nat. Rev. Mol. Cell Biol.*, 2014; Collinet et al., *Nat. Cell Biol.*, 2015; Heller et al., *Dev. Cell*, 2014] behaviors are physiologically functional and often arise through differentiation from its sisters or cousins since its ancestral division [Le Clainche et al., *Physiol. Rev.*, 2008; Rose et al., *WormBook*, 2014; Maduro, *Semin. Cell Dev. Biol.*, 2017; Jankele et al., *eLife*, 2021; Qiu et al., *Cell*, 2024; Chen et al., *eLife*, 2025], further sublineage-wise comparison in global proves that such morphological differentiation can be distinguished statistically (Figure 1G and 1H). In other words, cells sharing the same ancestor with different levels of division asymmetry can be distinguished statistically, exemplified by EMS and P2 derived from P1 cell (Figure 1G); cells sharing the same ancestor with different levels of intercalation depth can be distinguished statistically, exemplified by hypodermis and neurons derived from C lineage (Figure 1H). Together, these results establish the 12 morphology descriptors as accurate quantitative metrics for characterizing not only individual cellular states but also differentiation between distinct cellular states.

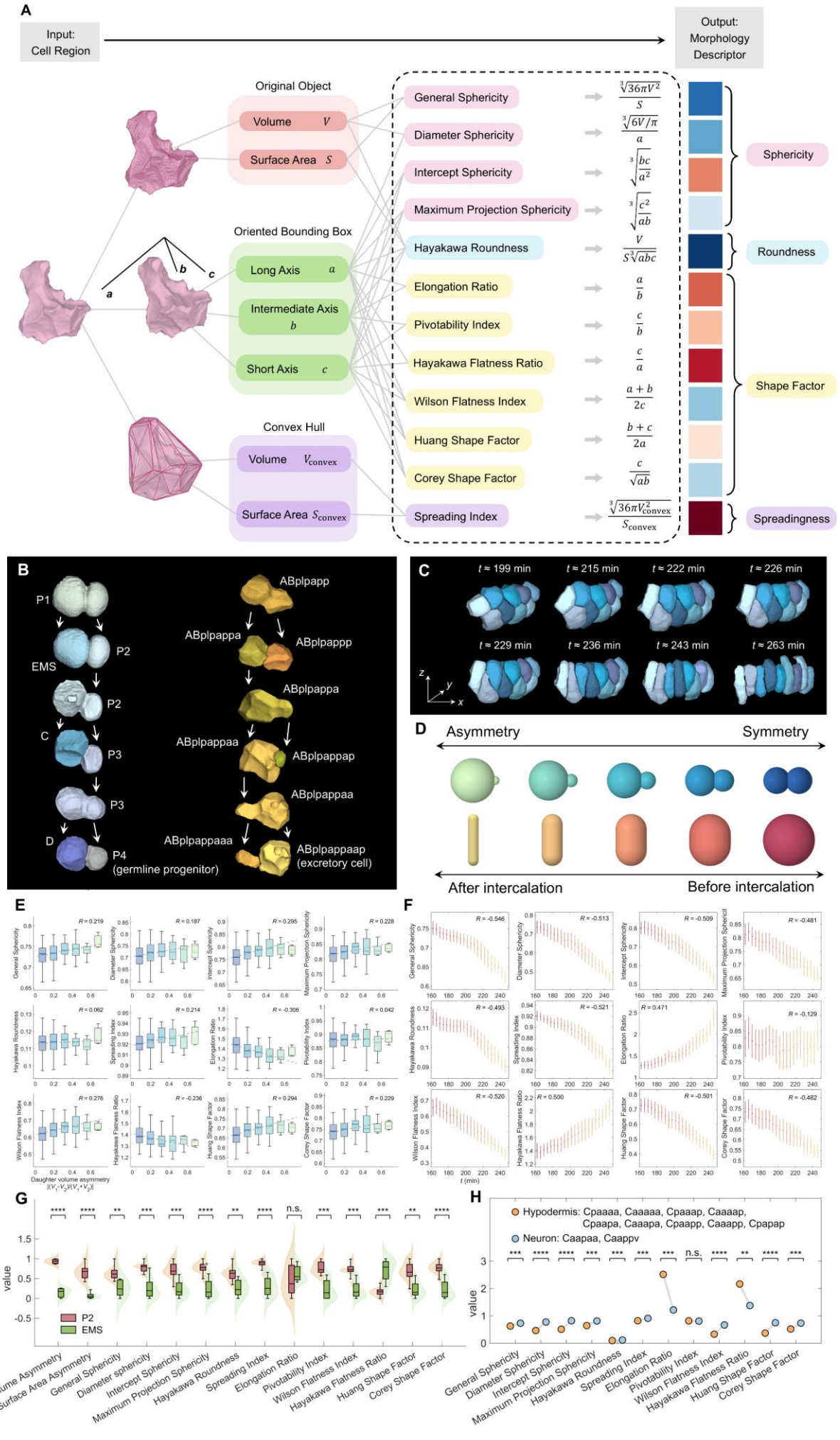

Figure 1. 3D morphology descriptors can characterize various cellular states quantitatively. (A) Quantification pipeline taking 3D cell regions as input and 3D morphology descriptors as output. (B) Representative morphologies of dividing cells with high division asymmetry. (C) Representative morphologies of intercalating cells with increasing intercalation depth. (D) Mathematical models of dividing cells with varied division asymmetry (top) and intercalating cells with varied interaction depth (bottom), with details in METHOD DETAILS. (E) Change of cell morphology descriptors over daughter size asymmetry (daughter volume asymmetry), with the ones over daughter surface area asymmetry in Figure S2. (F) Change of morphology descriptors over intercalation depth (developmental time, using the last moment of 4-cell stage as time zero). (G) Distribution of size asymmetry and morphology descriptors (linearly normalized to place the two metric types on a comparable scale) of the asymmetrically dividing cell (P2) and its sibling (EMS), revealing 11 morphology descriptors that significantly distinguish them as two differentiated sublineages. (H) Distribution of morphology descriptors of the intercalating cells (hyperdermis) and their siblings (neurons), revealing 11 morphology descriptors that significantly distinguish them as two differentiated sublineages.

Cell morphology variation is robust against mechanical compression and regulated by Notch signaling.

Provided the 12 validated quantitative 3D cell morphology descriptors, we first revisited the classic question of developmental variation among individual embryo samples, where prior efforts have been made to examine the variation of cell division timing and cell cycle length [Schnabel et al., *Dev. Biol.*, 1997], cell division orientation [Richards et al., *Dev. Biol.*, 2013], cell positions [Moore et al., *Development*, 2013], cell size [Arata et al., *Front. Physiol.*, 2015], cell-cell contact relationship and contact area [Azuma et al., *Front. Bioinform.*, 2023], and so on and so forth. Here, we utilized two public datasets of *C. elegans* embryogenesis that contain time-lapse 3D fluorescence images (green fluorescent protein labeling cell nuclei for cell lineage tracing; mCherry labeling cell membranes for cell morphology segmentation) along with 809,718 3D cell regions in total within embryos under natural condition (8 individual embryo samples), with mechanical compression (17 individual embryo samples), and with Notch signaling blocked (2 individual embryo samples) (Figure 2A; Supplementary Data 1) [Cao et al., *Nat. Commun.*, 2020; Guan et al., *Nat. Commun.*, 2025]. For each 3D cell morphology descriptor, the variation coefficient is calculated for every unique cell using its values across individual embryo samples, then averaged over all unique cells at each moment over development. Intriguingly, natural and mechanically compressed embryos exhibit comparable variation across all 3D cell morphology descriptors, with an average relative change of <12% at 150 minutes after the last moment of the 4-cell stage (Figure 2B and 2C); this robustness may reflect fail-safe mechanisms (*e.g.*, compensatory cell movements proposed before) that mitigate the effects of mechanical compression *in utero*, particularly in old or starved adults [Jelier et al., *Cell Syst.*, 2016; Pimpale et al., *eLife*, 2020]. In contrast, genetically perturbed embryos with RNAi against *lag-1* (terminal effector

of the Notch signaling pathway) exhibit elevated variation across all 3D cell morphology descriptors, with an average relative elevation >24% at 150 minutes after the last moment of the 4-cell stage (Figure 2F and 2G); this suggests an underexplored role for the Notch signaling pathway in regulating cell morphology, extending beyond its well-explored role in regulating gene expression [Priess, *WormBook*, 2005; Greenwald & Kovall, *WormBook*, 2013]. These comparative conclusions still hold when variation is calculated using alternative sample groups and sizes across all three experimental conditions (Figure S3).

To test the hypothesis that variation in cell morphology propagates to that in cell-cell contact (which has been known to be critical for signaling transduction and cell division), we evaluate the cell-cell contact area variation of natural, mechanically-compressed, and signaling-blocked embryos [Mello et al., *Cell*, 1994; Goldstein, *J. Cell Biol.*, 1995; Mickey et al., *Development*, 1996; Sugioka & Bowerman, *Dev. Cell*, 2018]. Consistent with the cell morphology descriptor, the variation level remains comparable before and after mechanical compression, but is significantly elevated by roughly 37.1% at 150 minutes after the last moment of the 4-cell stage, when Notch signaling is blocked (Figure 2D and 2H). To check if the cell-cell-contact-based developmental mechanisms (*e.g.*, Notch signaling) are violated, we still use the Notch signaling target and excretory cell progenitor ABplpapp as example, which shows similar contact relationship and area to neighbor cells (goodness of fit = 0.732) before and after mechanical compression (Figure 2E); however, when Notch signaling is blocked, violation emerges with many contacts lost (*incl.*, MSapap, MSappa), added (*incl.*, ABalppap, ABalpppa, ABplapppp, ABplpaapa, ABplpaapp, ABplpapap, Eala, Eara), or with very different areas (*incl.*, ABalpppp, ABplpaap, ABplpaapp, ABplppp, Eal, Ealp, MSapap, MSapp, MSappa) (Figure 2I-2K). Such a discrepancy is biased to contact accumulation to ABpl sublineage/colony and far away from MSa sublineage/colony (Figure 2I-2K), adding up a secondary violation to signaling transduction (spatial scale) beyond the genetic perturbation (molecular scale) itself. Moreover, this violation continues in ABplpapp cell's daughter ABplpappa (Figure S4A-S4D) and granddaughter ABplpappaa (Figure S4E-S4H), which are supposed to receive Notch signaling but lose contact with the original signaling cells. In summary, the Notch signaling not only functions at the genetic level through its ligand-receptor-transcriptional cascade, but also molds cell positions, cell morphologies, and cell-cell contact relationships and areas that are required by the signaling and responding cells.

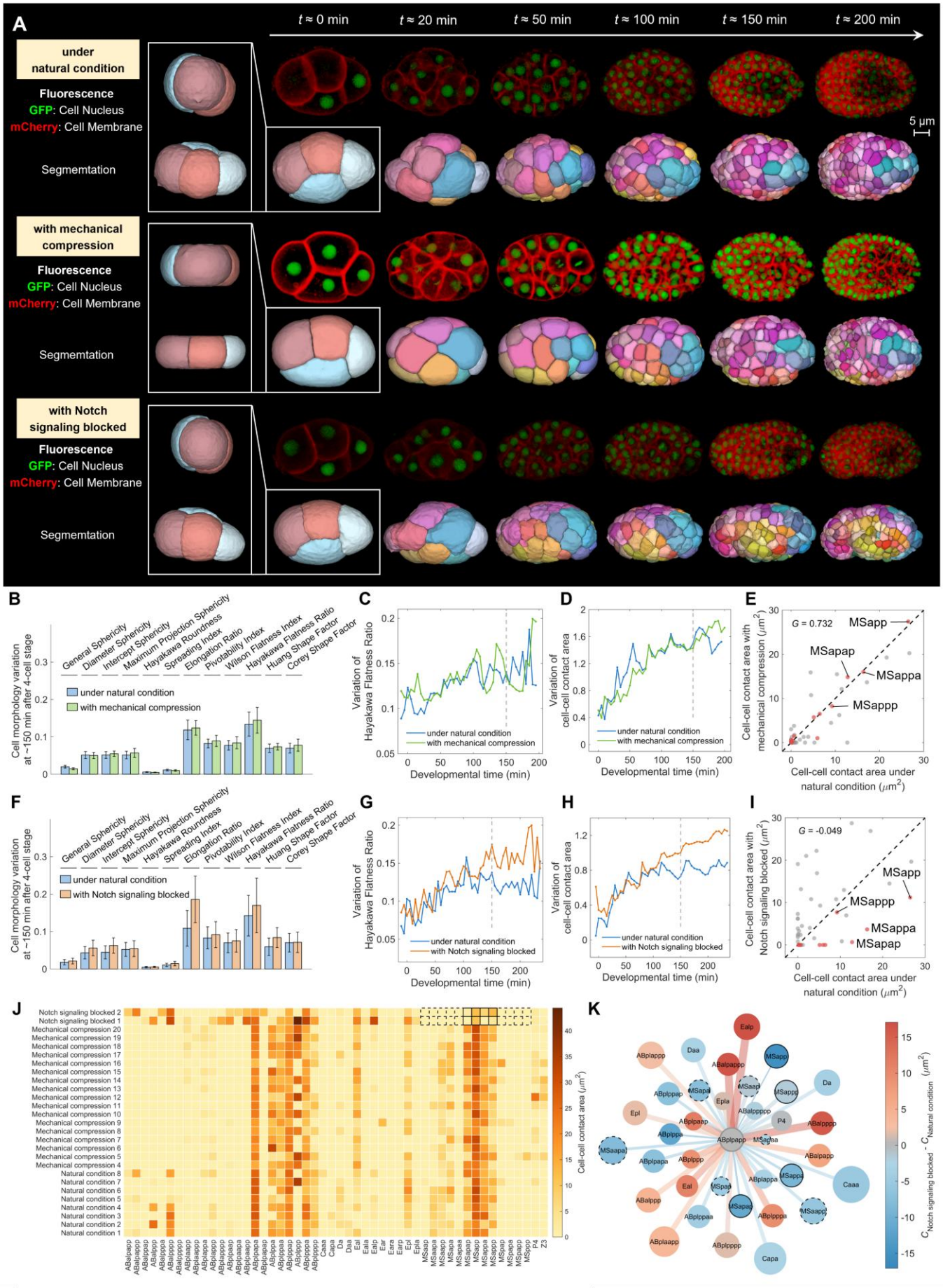

Figure 2. Cell morphology variation is well controlled during *C. elegans* embryonic development, remaining robustness with mechanical compression but not with Notch signaling blocked. (A)

Fluorescence (top) and segmentation (bottom) images of *C. elegans* embryos in natural condition (1st panel), with mechanical compression (2nd panel), and with Notch signaling blocked (3rd panel). (B) Distribution (mean ± standard deviation) of cell morphology variation at 150 minutes after the last moment of 4-cell stage, revealing a similar cell morphology variation level (compared to the embryos under natural condition) in the embryos with mechanical compression. (C) Similar cell morphology (exemplified by Hayakawa Flatness Ratio) variation level (compared to the embryos under natural condition) in the embryos with mechanical compression over developmental time (using the last moment of 4-cell stage as time zero). (D) Similar cell-cell contact area variation level (compared to the embryos under natural condition) in the embryos with mechanical compression over developmental time (using the last moment of 4-cell stage as time zero). (E) Comparison of cell-cell contact area between embryos under natural condition and with mechanical compression, centering the Notch signaling target and excretory cell progenitor ABplpapp and highlighting the previously reported Notch signaling cells in MS lineage. (F) Distribution (mean ± standard deviation) of cell morphology variation at 150 minutes after the last moment of 4-cell stage, revealing an elevating cell morphology variation level (compared to the embryos under natural condition) in the embryos with Notch signaling blocked. (G) Elevating cell morphology (exemplified by Hayakawa Flatness Ratio) variation level (compared to the embryos under natural condition) in the embryos with Notch signaling blocked over developmental time (using the last moment of 4-cell stage as time zero). (H) Elevating cell-cell contact area variation level (compared to the embryos under natural condition) in the embryos with mechanical compression over developmental time (using the last moment of 4-cell stage as time zero). (I) Comparison of cell-cell contact area between embryos under natural condition and with Notch signaling blocked, centering the Notch signaling target and excretory cell progenitor ABplpapp and highlighting the previously reported Notch signaling cells in MS lineage. (J) Cell-cell contact area in *C. elegans* embryos under natural condition (8 individual samples), with mechanical compression (17 individual samples), and with Notch signaling blocked (2 individual samples), centering the Notch signaling target and excretory cell progenitor ABplpapp and highlighting the previously reported Notch signaling (solid boundary) and non-signaling (dashed boundary) cells in MS lineage. (K) Change of cell-cell contact area, centering the Notch signaling target and excretory cell progenitor ABplpapp and highlighting the previously reported Notch signaling (solid boundary) and non-signaling (dashed boundary) cells in MS lineage, where the circle area and band width are positively associated with cell volume and cell-cell contact area in embryos under natural condition.

High-throughput scan of differential cell morphologies and gene expressions unveils their dynamic decoupling and coupling.

Cell morphology represents a complex outcome of both intracellular (*e.g.*, cytoskeleton and actomyosin activities) and extracellular (*e.g.*, cell mechanics and signaling) processes [Fletcher et al., *Nature*, 2010]. Nevertheless, they are ultimately encoded — directly or indirectly — by the differential

spatiotemporal gene expressions that unfold during embryogenesis beginning from a single-cell zygote [Guan et al., *bioRxiv*, 2019; Xiong et al., *Genetics*, 2025]. While previous correlation analyses of cell morphology and gene expression mainly relied on 2D cell projections or crosssections, a comprehensive analysis that fully extracts information from complete 3D cell morphologies is still lacking [Benkeder et al., *eLife*, 2025; Ramezani et al., *Nat. Methods*, 2025]. Inspired by the global and local correlations between cell morphology and gene expression demonstrated above (Figure 2), we integrate the morphology descriptors with extensive cell-lineage-resolved gene expression profiles previously published [Murray et al., *Genome Res.*, 2012; Huang et al., *Bioinformatics*, 2017; Chen et al., *Genetics*, 2018; Packer et al., *Science*, 2019; Guan et al., *Dev. Genes Evol.*, 2020; Ma et al., *Nat. Methods*, 2021; Guan et al., *Nat. Commun.*, 2025]. This standardized dataset (accessible via the *CMOS* website [https://bcc.ee.cityu.edu.hk/cmos; Guan et al., *Nat. Commun.*, 2025]) encompasses 412 key genes (either playing critical roles in development, showing evolutionary conservation in complex organisms like humans, or remaining to be functionally characterized) across 392,541 independent 3D cell objects, ~65 million data points.

Within the *C. elegans* embryonic cell lineage tree documented from the 1-cell to >550-cell stages (covering 96.05% of all embryonic cells) [Guan et al., *Nat. Commun.*, 2025], we compute each cell's temporal trajectories averaged over all embryo datasets with cell morphological and gene expression data, resulting in 276,316 temporal trajectories in total (Supplementary Data 2). We focused on the continuously dividing cell with both morphological and genetic profiles recorded in it as well as its two daughter cells and four granddaughter cells in the two sublineages produced (Figure 3A). For each gene expression profile normalized between 0 and 1 across embryogenesis, the average expression of each and every descendant in two sublineages is required to exceed 0.2, mitigating the potential noise due to cell imaging, tracking, *etc.* For both cell morphology and gene expression, we identify the differentiation between sublineages by all their cells' time-series data using a two-sample *t*-test ($p < 0.1$) and quantify its level with normalized asymmetry values $A_{\mathrm{M}} = \frac{M_1 - M_2}{M_1 + M_2}$ (M_1: cell morphology value averaged over all cells in Sublineage 1 and all their time points; M_2: cell morphology value averaged over all cells in Sublineage 2 and all their time points) and $A_{\mathrm{G}} = \frac{G_1 - G_2}{G_1 + G_2}$ (G_1: gene expression value averaged over all cells in Sublineage 1 and all their time points; G_2: gene expression value averaged over all cells in Sublineage 2 and all their time points), resulting in 25,097 differentiation events in total (Supplementary Data 3). Coupled and decoupled relationships between specific morphology descriptors (12 in total) and gene expressions (412 in total) are characterized by detecting their co-asymmetry across unique cells, resulting in 224,988 coupled events and 1,428 decoupled events in total; the consequent co-asymmetry frequency further quantifies how broadly the coupling exists (Supplementary Data 4).

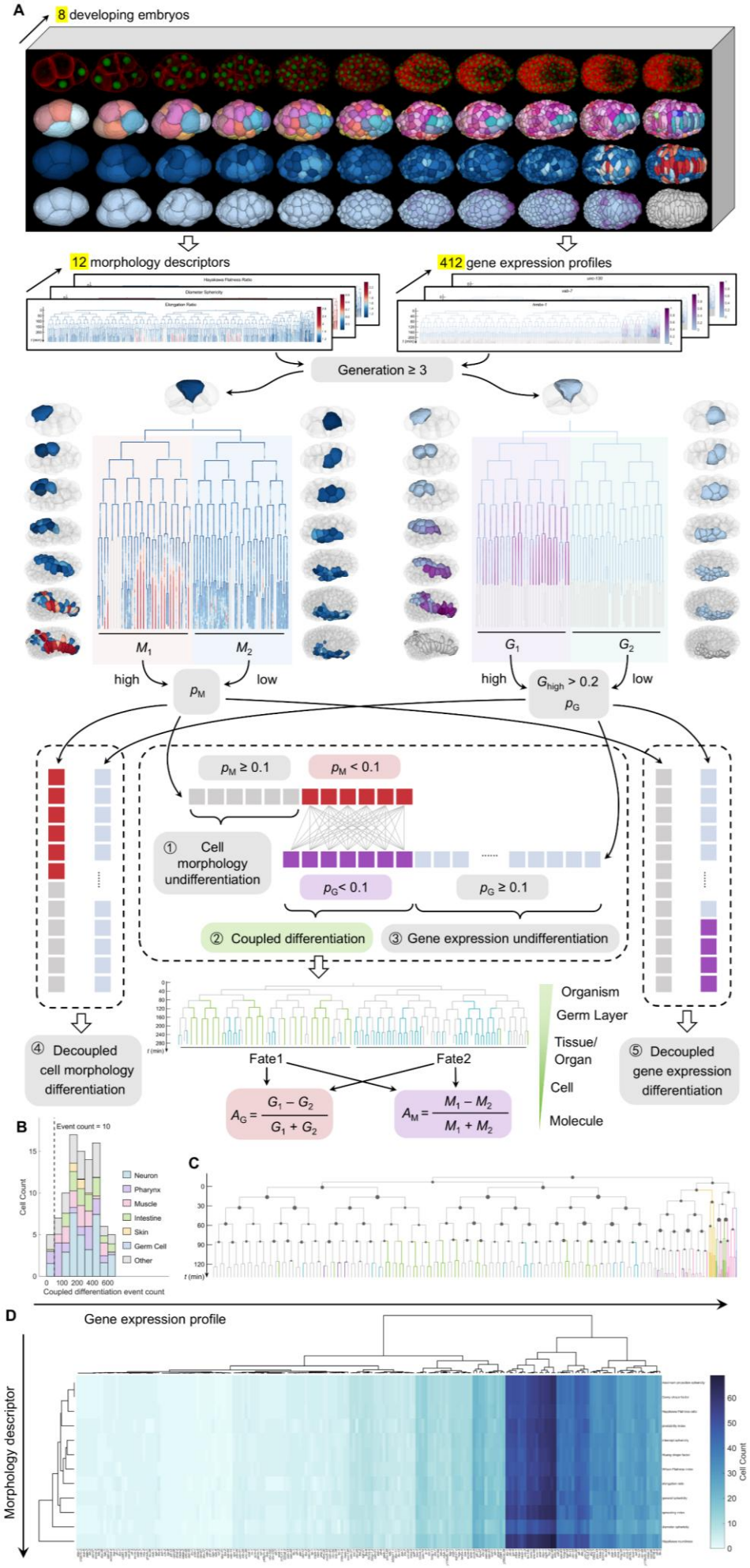

Figure 3. Cell morphology and gene expression differentiations can be coupled or decoupled. (A) Automatic workflow for detecting sublineage-wise differentiation events across 12 cell morphology descriptors and 412 gene expression profiles mapped onto the embryonic lineage tree, with A_{M} and A_{G} denoting asymmetry level and p_{M} and p_{G} denoting statistical significance, respectively. (B) Count of unique cells exhibiting coupled differentiation between cell morphology and gene expression, covering all major cell fates. (C) Lineal position of unique cells detected exhibiting coupled differentiation between cell morphology and gene expression, covering all major lineage parts. (D) Clustering (based on agglomerative hierarchical clustering) of coupled differentiation events between paired cell morphology descriptors and gene expression profiles.

Sublineage-wise asymmetry scans of 12 cell morphology descriptors and 412 gene expression profiles identified 122 cells with differential morphology descriptors and 105 unique cells with differential gene profiles, whereas 95 unique cells with differentiation in both aspects (Table S2). The differential gene expression profiles detected between sublineages of a given cell list, as reported in a recent summary, are consistent with prior knowledge, thereby validating our computational pipeline (Table S3) [Murray et al., *Genome Res.*, 2012; Zacharias et al., *PLoS Genet.*, 2015; Packer et al., *Science*, 2019; Ma et al., *Nat. Methods*, 2021; Murrar et al., *PLoS Genet.*, 2022; Liu et al., *Genetics*, 2023]. Remarkably, although differential gene expression is well recognized for its role in cell fate specification [Du et al., *Dev. Cell*, 2015; Santella et al., *Nucleic Acids Res.*, 2016; Du et al., *Cell*, 2014], the frequent co-differentiation of cell morphology and gene expression reveals an underexplored coupling between them, which orchestrates morphogenesis spanning cellular to organismal scales. Regardless of its cellular frequency, such co-differentiation generally participates in the cell fate specification of neuron, pharynx, muscle, intestine, skin, germline, and others across the whole lineage (Figure 3B and 3C). The overall clustered frequency of co-differentiation between cell morphology and gene expression (agglomerative hierarchical clustering [Murtagh & Contreras, *WIREs Data Mining and Knowledge Discovery*, 2012]) highlights a subset of genes ($172/412 \approx 41.75\%$) detected with coupling to all morphology descriptors; this subset includes major tissue- and organ-specific transcriptional markers conserved between worms and humans, further supporting a general coordination between cell fate specification and morphogenesis down to cellular scale (Figure 3D) [Murray, *Wiley Interdiscip. Rev. Dev. Biol.*, 2018]. In addition, cells with morphological but not genetic differentiation may be influenced by spatial, temporal, or mechanical cues; for instance, even with similar levels of stiffness or surface tension oscillating over cell cycle, larger cells tend to be more spherical [Fujii et al., *Commun. Biol.*, 2021; Guan et al., *Commun. Nonlinear Sci. Numer. Simul.*, 2023], warranting further cellular mechanical property inference and analysis [Ichbiah et al., *Nat. Methods*, 2023; Vanslambrouck et al., *PLoS Comput. Biol.*, 2024; Yamamoto et al., *bioRxiv*, 2025]. In line with recent studies of mammalian development [Pineau et al., *Development*, 2025; Bennabi et al., *Sci. Adv.*, 2025], these categories suggest that diverse regulatory mechanisms are encoded in developing systems with varying complexities.

Endodermal, mesodermal, and ectodermal cells display significantly distinct morphological and genetic signatures during differentiation.

To elucidate how cell morphology and gene expression are coupled or decoupled during development, we examined whether these signatures differentiate together or independently along the hierarchical trajectory of cell fate specification — from germ layer segregation to tissue/organ formation, and ultimately to fine-grained, function-specific cells within individual tissue/organ. Germ layer segregation is one of the earliest conserved milestones in metazoan development, giving rise to the endoderm, mesoderm, and ectoderm, which serve as progenitors for diverse cell fates and define the spatial framework of the developing organism [Farrell et al., *Science*, 2018; Rossant et al., *Dev. Cell*, 2022]. During *C. elegans* embryonic development, processes such as asymmetric cell division, intercellular signaling, and movement give rise to the endoderm (producing intestine cells), mesoderm (producing neuron, muscle, pharynx), and ectoderm (skin) [Leung et al., *Dev. Biol.*, 1999; Nance et al., *WormBook*, 2005]. Here, we adopted the cell fate annotations summarized in previous studies [Sulston et al., *Dev. Biol.*, 1983; Ma et al., *Nat. Methods*, 2021; Guan et al., *Nat. Commun.*, 2025], which classify major somatic cell fates into neuron, pharynx, muscle, skin, intestine, and others, including germline cells (P0, P1, P2, P3, P4), excretory cell (ABplpappaap), and unspecified progenitors whose descendants can give rise to multiple somatic fates, *etc*. With these clear cell fate classifications, we next investigated whether pairs of sublineages undergoing germ layer segregation exhibit coupled or decoupled patterns regarding cell morphology and gene expression.

First, we examined differentiation between the mesoderm and endoderm utilizing the six generations of the EMS (the second somatic founder cell in *C. elegans* development, derived from the second round of asymmetric cell division post fertilization) lineage. Its anterior sublineage (MS) predominantly differentiates into mesodermal fates (32.98% pharynx and 29.79% muscle) and posterior sublineage (E) exclusively differentiates into endodermal cells (100% intestine) (Figure 4A and 4B). In terms of gene expression, we compare the mesodermal descendants (pharynx and muscle) of MS and the endodermal descendants of E, revealing a complete segregation between mesoderm and endoderm gene sets. These clearly partitioned gene sets include but are not limited to the known markers (*e.g.*, *elt-2*, *end-1*, and *nhr-102* for endoderm; *afft-2*, *moe-3*, and *ceh-21* for mesoderm), in agreement with the prior knowledge of the mutual inhibition pathway mediated by Wnt signaling and providing new resources for gene function identification (Figure 4C and 4D) [Lee et al., *Curr. Biol.*, 2006; Zacharias et al., *PLoS Genet.*, 2015]. Within the mesoderm, the pharyngeal-specific (*e.g.*, *tbx-7*, *pha-4*, and *hmbx-1*), muscle-specific markers such as *tbx-8*, *hlh-1*, and *unc-120* (Figure 4C and 4D, in agreement with the progressively bifurcation conceptualized by the Waddington landscape and providing new resources for gene function identification [Waddington, *Routledge*, 1957]. Representative gene expression profiles illustrating antagonism between

mesoderm and endoderm, antagonism between neuron and pharynx, and overlap between neuron and pharynx are shown in Figure 4G. In terms of cell morphology, six morphology descriptors revealed significantly distinct between endodermal and mesodermal cell populations, no matter if neuronal or pharyngeal cells were specified (Figure 4E). Representative cell morphology descriptor (Elongation Ratio) illustrating more elongated neuron and muscle cells and more angular intestine cells are shown in Figure 4F.

Second, we test the differentiation between ectoderm and mesoderm using the seven generations of C lineage (the third somatic founder cell of embryogenesis derived from the third rounds of asymmetric cell division), which gives rise to left(Ca)-right(Cp) symmetric fates. The anterior sublineages (Caa and Cap) dominantly turn into mesodermal fates (81.25% for skin) and the posterior sublineages (Cap and Cpp) exclusively develop into mesoderm fate (100% for muscle) (Figure 4H and 4I). Taking the major mesodermal pharynx and muscle in MS to compare with the endoderm cell fates in E, in the gene expression aspect, a complete exclusion between mesoderm and endoderm gene sets are found, including known general markers for both (*e.g.*, *elt-2*, *end-1*, and *nhr-102* for endoderm; *afft-2*, *moe-3*, and *ceh-21* for mesoderm) (Figure 4J and 4K), in match to the prior knowledge mutual inihibition pathway activated by Wnt signaling. In addition to the shared gene pool within the mesoderm, the specific cell types, a considerable number of genes were identified to demonstrate fate-specific expression patterns: pharyngeal-specific markers like *tbx-7*, *pha-4*, and *hmbx-1*; muscle-specific markers such as *tbx-8*, *hlh-1*, and *unc-120* (Figure 4J and 4K), in match to the prior knowledge of progressively bifurcated differentiation noted by Waddington landscape. Representative gene expression profiles showing antagonism between ectoderm (skin) and endoderm (muscle) and sharing between them are shown in Figure 4N. For the aspect of cell morphology, except the General Sphericity and Hayakawa Roundness, the remaining ten morphology descriptors reflect significant difference between the mesodermal and ectodermal cell as well as their lineage origin (Figure 4L), specifically highlighting the morphological difference between them (exemplified by the Maximum Projection Sphericity in two pairs of cells showing the skin cell tend to be elongated and muscle cell tend to be rectangular, Figure 4M).

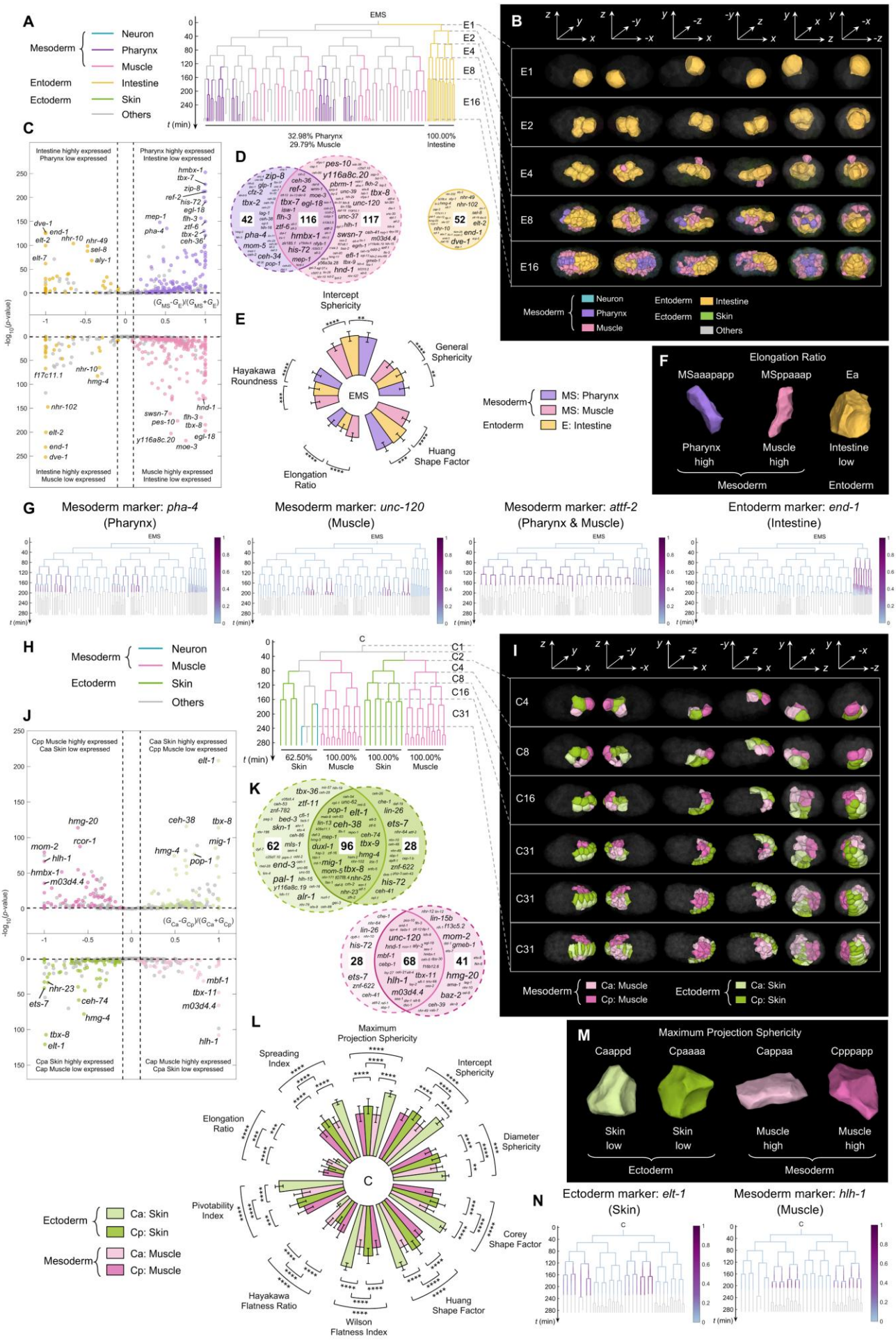

Figure 4. Cell morphology and gene expression differentiations distinguish cell fates between germ layers. (A) Cell fate pattern of the EMS lineage. (B) Cell morphology distribution of the EMS lineage illustrated in 3D space, showing stereotyped spatiotemporal patterns of EMS-derived mesoderm (neuron and pharynx) and endoderm (intestine). (C) Distribution of asymmetry level (A_{G}) and statistical significance (p_{G}) in gene expression differentiation distinguishing EMS-derived endoderm vs. mesoderm and pharynx vs. muscle within the mesoderm. (D) Venn diagram of gene markers distinguishing mesoderm vs. endoderm and pharynx vs. muscle within the mesoderm. (E) Distribution of asymmetry level (A_{M}) and statistical significance (p_{M}) in cell morphology differentiation distinguishing EMS-derived endoderm vs. mesoderm and pharynx vs. muscle within the mesoderm. (F) Representative morphologies of EMS-derived mesoderm (neuron and pharynx) and endoderm (intestine) cells, displaying distinct values in cell morphology descriptors. (G) Gene expression distribution of EMS lineage illustrated in lineage tree, showing gene markers distinguishing endoderm vs. mesoderm and pharynx vs. muscle within the mesoderm. (H) Cell fate pattern of the C lineage. (I) Cell morphology distribution of the C lineage illustrated in 3D space, showing stereotyped spatiotemporal patterns of C-derived ectoderm (skin) and mesoderm (muscle). (J) Distribution of asymmetry level (A_{G}) and statistical significance (p_{G}) in gene expression differentiation distinguishing C-derived ectoderm vs. mesoderm. (K) Venn diagram of gene markers distinguishing mesoderm vs. endoderm and pharynx vs. muscle within the mesoderm. (L) Distribution of asymmetry level (A_{M}) and statistical significance (p_{M}) in cell morphology differentiation distinguishing C-derived ectoderm vs. mesoderm. (M) Representative morphologies of C-derived ectoderm (skin) and endoderm (muscle) cells, displaying distinct values in cell morphology descriptors. (N) Gene expression distribution of C lineage illustrated in lineage tree, showing gene markers distinguishing C-derived ectoderm vs. mesoderm.

Cell-fate-specific morphological features allow sensitive reverse prediction.

Gene expression has long been used as a marker for cell fate distinguishment between neuron, pharynx, muscle, intestine, *etc.* [Ma et al., *Nat. Methods*, 2021; Cole et al., *eLife*, 2024], which is captured by our data of 412 genes, through calculating the cellular frequency with substantial sublineage asymmetry (Figure 5A and 5B, Figure S5, Table S4). Provided that the cell morphology could be coupled with gene expression (Figure S6, Figure S7), we wonder if an equivalent identifier could be established solely based on cell morphology. To this end, we focus on the five major somatic cell fates derived from the three germ layers and outline their cell morphology descriptor distributions using 352,629 3D cell objects in 8 natural embryos. Remarkably, each cell fate carries obviously different distributions compared to others; for example, neuron cells have high values in almost all morphology descriptors except Elongation Ratio and Hayakawa Flatness Ratio (reflecting their round and smooth shape), conversely, skin cells have high values in those two morphology descriptors (reflecting their elongated long axis and two short axes of similar length) (Figure 5C, Figure S8). We also investigated whether distinct cell fates could be distinguished based

on morphology descriptors. Most importantly, although different morphology descriptors have different sensitivities and sample size reliance to distinguish a pair of cell fates as expected, the best morphology descriptor always requires a sample size in the magnitude of dozens to significantly (two-sample *t*-test, $p < 0.1$) distinguish any pairwise cell fates (Figure 5D-5F; Figure S9; Figure S10). For instance, the significant distinction between neuron and intestine only requests a sample size of 13 cells via Hayakawa Roundness, while the significant distinction between muscle and intestine requests the largest sample size of 91 cells via Elongation Ratio (Figure S10). This considerable sample size in dozens indicates the power of cell-morphology-based cell fate distinguisher, as most biomedical sceniros produce much more cell object data. As a sneak peek, *C. elegans* embryo ends with ~550 cells, human embryoid ends with ~2,000 cells with axial establishment [Moris et al., *Nature*, 2020], and blood extraction takes billions of cells in one shot [Dean L., *Blood Groups and Red Cell Antigens*, 2005].

To further investigate whether cells within the same tissue/organ but with more differentiated fates could be distinguished by morphology descriptors, we take the ABarp lineage as an example, considering that it produces dorsal hypodermis (ABparpaa sublineage, constituting the anterior of the dorsal midline) and seam cells (ABarpap and ABarpp sublineages, constituting on the left and right side of the dorsal midline with bilateral symmetry) to compose the skin (Figure 5G and 5H) [Chisholm & Hardin, *WormBook*, 2005; Walck-Shannon et al., *Nat. Rev. Mol. Cell Biol.*, 2014]. Morphology descriptors including Hayakawa Roundness, Diameter Sphericity, Elongation Ratio consistently show that the dorsal hypodermal cells are significantly deviated from seam cells with the same trend regardless of their lineal origin, supporting the applicability of cell morphology descriptors (Figure 5I and 5J). Qualatively, sorsal cells elongate across the dorsal midline during intercalation, resulting in a columnar arrangement, while seam cells remain comparatively shorter and less elongated, which may give rise to additional elongation of long axis of dorsal cells. Such differential cell morphologies are also coupled with differential gene expression exemplified by *tbx-8* and *tbx-9* highly expressed in dorsal hypodermis and *ets-7*, *glp-1*, and *lag-1* highly expressed in seam cells (Figure 6K). These findings pinpoint that the cell morphology can be extensively applied to more detailed cell fate specification, even within a general tissue/organ, just like the gene expression.

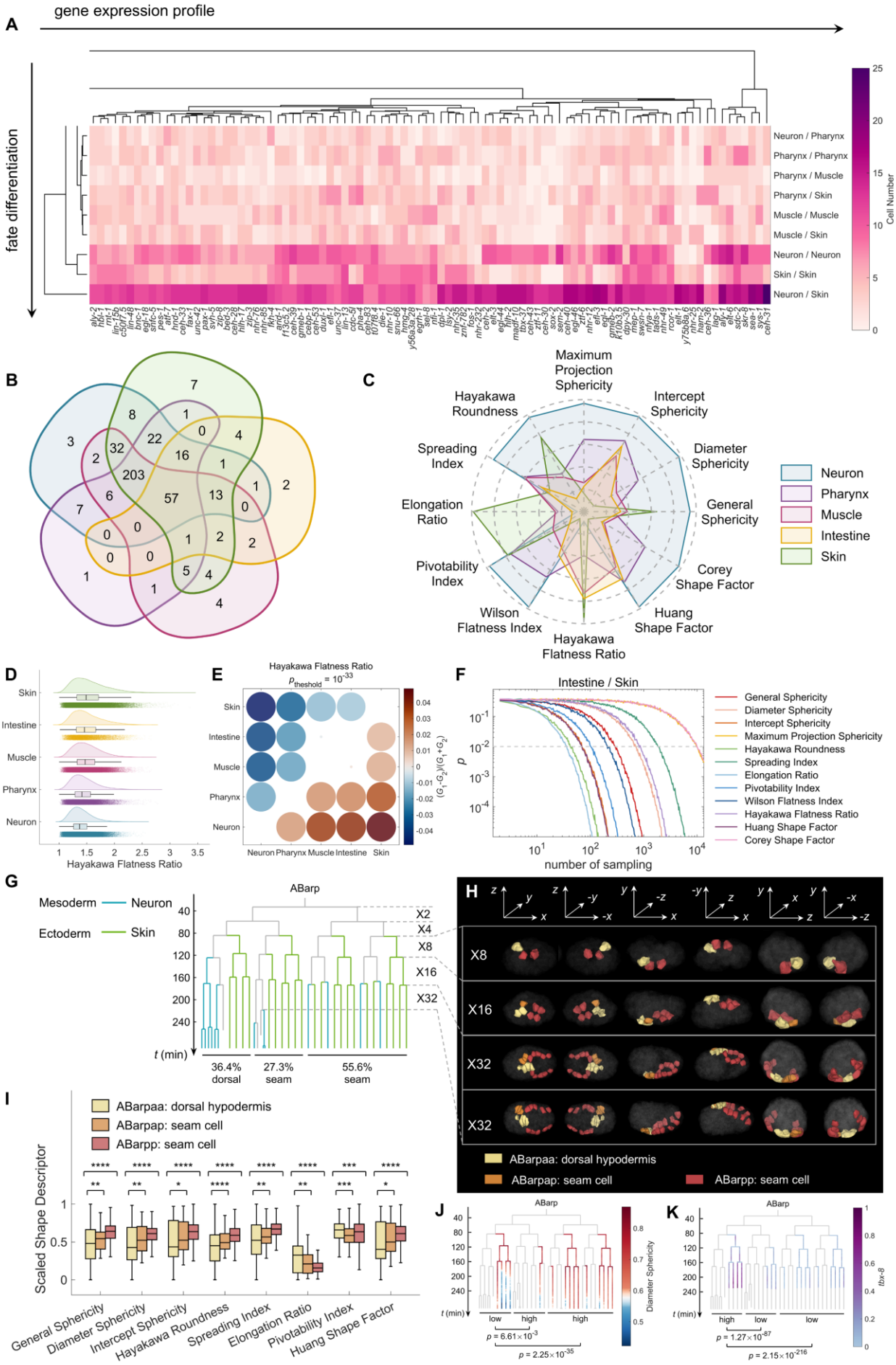

Figure 5. Cell morphology and gene expression differentiations distinguish cell fates among and within tissues/organs. (A) Clustering (based on agglomerative hierarchical clustering) of coupled

differentiation events between cell fate pairs and gene expression profiles. (B) Venn diagram of gene markers distinguishing neuron, pharynx, muscle, intestine, and skin [Liu, MATLAB Central File Exchange, 2025]. (C) Radar diagram of morphology descriptors distinguishing neuron, pharynx, muscle, intestine, and skin. (D) Distribution of values in cell morphology descriptors distinguishing neuron, pharynx, muscle, intestine, and skin, represented by Hayakawa Flatness Ratio. (E) Distribution of asymmetry level (A_{M}) and statistical significance (p_{M}) in cell morphology differentiation distinguishing neuron, pharynx, muscle, intestine, and skin, represented by Hayakawa Flatness Ratio. (F) Change of statistical significance (p_{M}) over cell region sample size for predicting differentiation between cell fate pairs, shown by all 12 cell morphology descriptors with different sensitivity levels. (G) Cell fate pattern of the ABarp lineage. (H) Cell morphology distribution of the ABarp lineage illustrated in 3D space, showing stereotyped spatiotemporal patterns of ABarp-derived dorsal hypodermis (ABarpaa sublineage) and seam cell (ABarpap and ABarpp sublineages). (I) Distribution of values in cell morphology descriptors distinguishing ABarp-derived dorsal hypodermis (ABarpaa sublineage) and seam cell (ABarpap and ABarpp sublineages), shown by all 8 cell morphology descriptors with sufficient statistical significance. (J) Cell morphology distribution of ABarp lineage illustrated in the lineage tree, showing morphology descriptor (represented by Diameter Sphericity) distinguishing ABarp-derived dorsal hypodermis vs. seam cell. (K) Gene expression distribution of ABarp lineage illustrated in lineage tree, showing gene marker (represented by *tbx-8*) distinguishing ABarp-derived dorsal hypodermis vs. seam cell.

Cell morphology within the same cell fate can differentiate over body axes.

Body axis establishment begins as early as the first few cell divisions after fertilization, rapidly setting up the anterior-posterior, left-right, and dorsal-ventral axes with differential gene expression [Lyczak et al., *Dev. Cell*, 2002]. These body axes subsequently guide the formation of tissues and organs — for example, the anterior and posterior ends of intestine must properly connect to the pharynx and rectum respectively, while undergoing body-axis-dependent coordinated elongation and twisting [Asan et al., *PLoS Genet.*, 2016; Cote et al., *bioRxiv*, 2025]. To determine whether axial bias influences morphology at the cellular level, we examined the body wall muscles, which are derived from the AB, MS, C, and D lineages and are assembled as staggered bilateral pairs across the four quadrants [Altun et al., *WormAtlas*, 2009].

Firstly, we examined differentiation between the dorsal and ventral muscles utilizing the five generations of the Cap lineage (Figure 6A and 6G). Its anterior sublineage (Capa) predominantly differentiates into ventral muscle cells (75%) and posterior sublineage (Capp) predominantly differentiates into dorsal muscle cells (87.5%) (Figure 6A). In terms of cell morphology, there are 6 cell morphology descriptors revealing significant differences between the ventral muscle cells of Capa and the dorsal muscle cells of Capp, among which Wilson Flatness Index shows the highest asymmetry level with $p = 4.37 \times 10^{-23}$ (Figure 6B, 6D and 6F). In terms of gene expression, two gene sets are coherently segregated (*e.g.*, *tlp-1* enriched in dorsal muscle cells and *swsn-7* enriched in ventral muscle cells) (Figure 6C and 6E).

Then, we examined differentiation between the left and right muscles utilizing the five generations of the D lineage (Figure 6H and 6N). Its anterior sublineage (Da) exclusively differentiates into left muscle cells (100%) and posterior sublineage (Dp) exclusively differentiates into right muscle cells (100%) (Figure 6H). In terms of cell morphology, there are 12 cell morphology descriptors revealing significant differences between the left muscle cells of Da and the right muscle cells of Dp, among which Wilson Flatness Index shows the highest asymmetry level with $p = 4.67 \times 10^{-5}$ (Figure 6I, 6K and 6M). In terms of gene expression, two gene sets are coherently segregated (*e.g.*, *ztf-6* enriched in left muscle cells and *efl-3* enriched in right muscle cells) (Figure 6J and 6L).

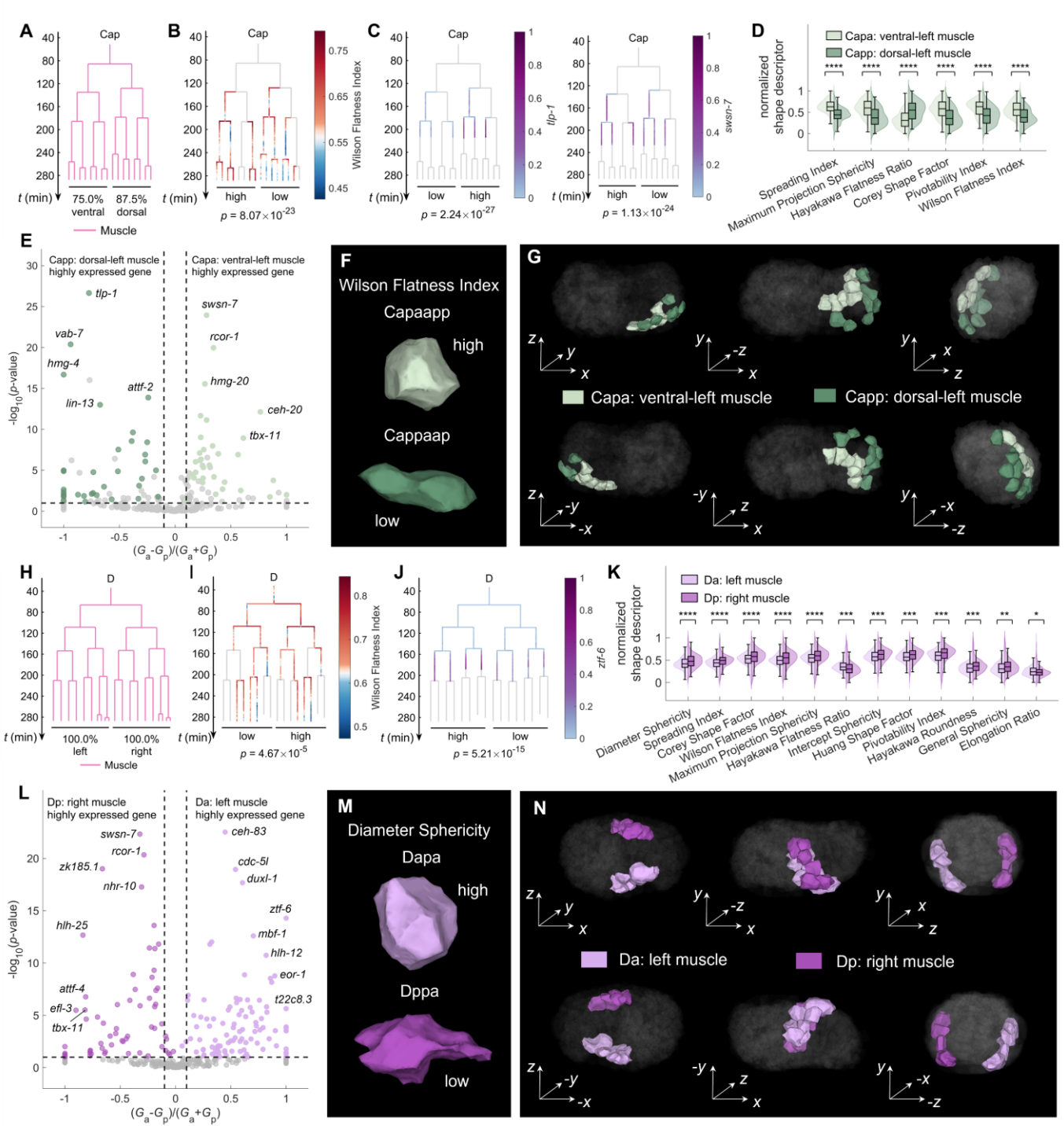

Figure 6. Cell morphology and gene expression differentiations distinguish cell fates along body axes.

(A) Cell fate pattern of the Cap lineage. (B) Cell morphology distribution of Cap lineage illustrated in the lineage tree, showing morphology descriptor (represented by Wilson Flatness Index) distinguishing Cap-derived ventral muscle vs. dorsal muscle. (C) Gene expression distribution of Cap lineage illustrated in lineage tree, showing gene markers (represented by *tlp-1* and *swsn-7*) distinguishing Cap-derived ventral muscle v.s. dorsal muscle, shown by all 6 cell morphology descriptors with sufficient statistical significance. (D) Distribution of asymmetry level (A_{M}) and statistical significance (p_{M}) in cell morphology differentiation distinguishing Cap-derived ventral muscle vs. dorsal muscle. (E) Distribution of asymmetry level (A_{G}) and statistical significance (p_{G}) in gene expression differentiation distinguishing Cap-derived ventral muscle vs. dorsal muscle. (F) Representative morphologies of Cap-derived ventral muscle vs. dorsal muscle, displaying distinct values in cell morphology descriptors (represented by Wilson Flatness Index). (G) Cell morphology distribution of the Cap lineage illustrated in 3D space, showing stereotyped spatiotemporal patterns of Cap-derived ventral muscle and dorsal muscle. (H) Cell fate pattern of the D lineage. (I) Cell morphology distribution of D lineage illustrated in the lineage tree, showing morphology descriptor (represented by Wilson Flatness Index) distinguishing D-derived left muscle vs. right muscle. (J) Gene expression distribution of D lineage illustrated in the lineage tree, showing gene marker (represented by *ztf-6*) distinguishing D-derived left muscle v.s. right muscle. (K) Distribution of asymmetry level (A_{M}) and statistical significance (p_{M}) in cell morphology differentiation distinguishing D-derived left muscle vs. right muscle. (L) Distribution of asymmetry level (A_{G}) and statistical significance (p_{G}) in gene expression differentiation distinguishing D-derived left muscle vs. right muscle. (M) Representative morphologies of D-derived left muscle vs. right muscle, displaying distinct values in cell morphology descriptors (represented by Diameter Sphericity). (N) Cell morphology distribution of the D lineage illustrated in 3D space, showing stereotyped spatiotemporal patterns of D-derived left muscle vs. right muscle.

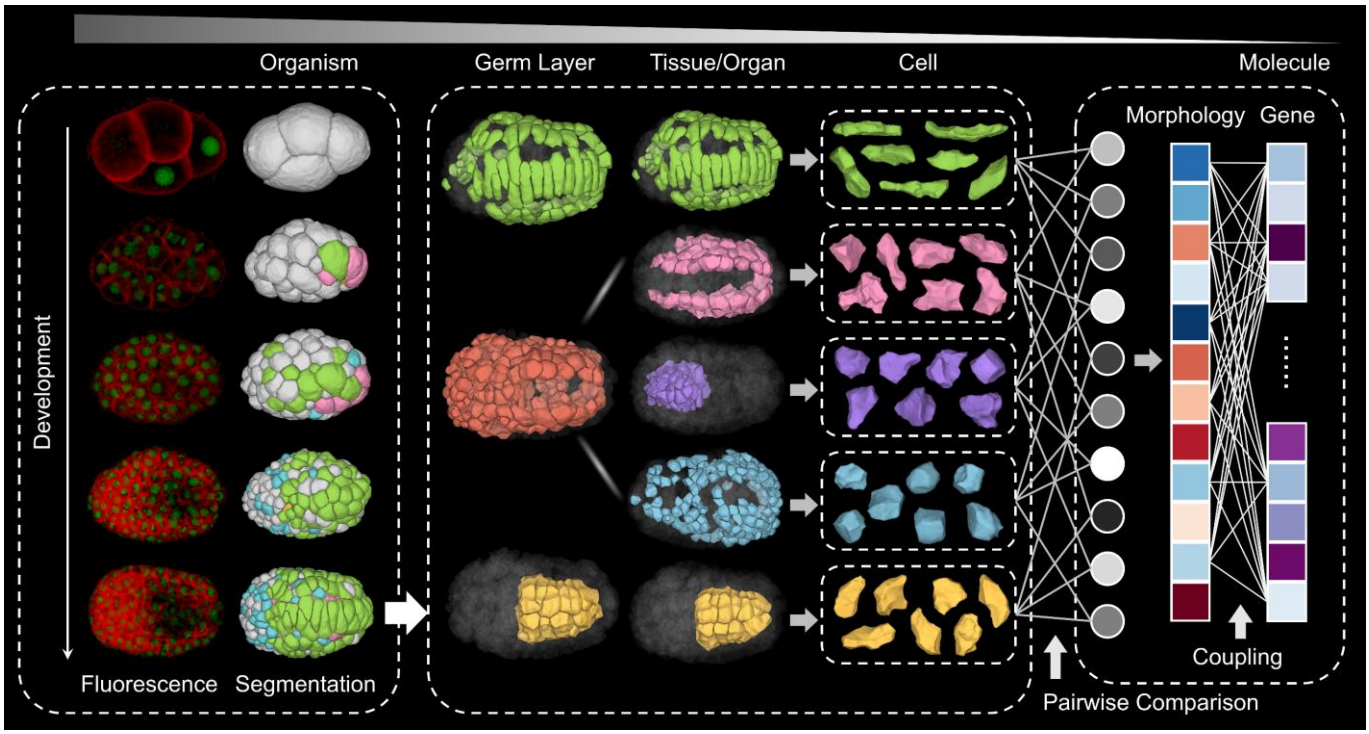

Figure 7. Conceptual summary of the developmental cell fate specification cascade, spanning organismal to molecular scales and driven by both coupled and decoupled differentiation of cell morphology and gene expression.

DISCUSSION

How cell fate specification is coupled to morphogenesis from cellular to organismal scales remains a central question in developmental biology, particularly in species with varying complexity. In this study, we demonstrate that 3D cell morphology descriptors quantitatively capture diverse cellular behaviors through both mathematical formulation and empirical validation (Figure 1; METHOD DETAILS). These morphological features are linked not only to dynamic cellular processes (*e.g.*, asymmetric division, intercalating movement, and neighbor contact) (Figure 2), but also to hierarchical differentiation spanning from germ layers (Figure 4) to tissues/organs (Figure 5) and cell-specific adjustments within them (*e.g.*, body-axis-dependent adjustment) (Figure 6). Global and local analyses reveal that cell morphologies are precise among individual embryos and robust to mechanical pressure, yet they rely critically on intercellular signaling, which governs contact relationships and areas essential for cell fate specification (Figure 2). Finally, high-throughput co-differentiation analyses between 12 cell morphology descriptors and 412 gene expression profiles uncover both decoupled and coupled regulatory mechanisms acting in concert to ensure precise developmental outcomes, consistent with previous findings (Figure 7) [Mestek Boukhibar et al., *Ann. Bot.*, 2016; Li et al., *Cell Rep.*, 2019; Xiao et al., *Cell Syst.*, 2022; Tian et al., *Phys. Biol.*, 2020].

Focusing on the 3D cell morphological dimension, we quantified a total of 809,718 cell objects and acquired 9,716,616 descriptor values across more than 27 *C. elegans* embryos, each reconstructed with complete whole-organism cell lineage traced. This high-quality dataset enables systematic analyses integrating gene expression, cell fate, cell identity, cell movement, mechanical states, signaling states, and other contextual features surrounding cell morphology (accessible via [https://www.dropbox.com/scl/fo/ynjioma2mfin454vyedwi/AMhusiAMIKter1YR9epx7c4?rlkey=15oji0q3w0c44aghy1afmu3wj&st=gvdsnu9m&dl=0]) [Cao et al., *Nat. Commun.*, 2020; Guan et al., *Membranes*, 2024; Guan et al., *Nat. Commun.*, 2025]. Such an informative resource provides a versatile platform for investigating a broad range of questions spanning from developmental biology to biophysics.

The integration of cell morphology and gene expression dimensions offers a novel framework for exploring the regulatory mechanisms of cell biology across molecular to organismal scales. It provides a powerful methodology and dataset that can be readily applied to a range of closely related fields.

(1) The successful application of 12 3D cell morphology descriptors in distinguishing differential gene expression as well as cell fate highlights the potential for expanding this framework to other types of 3D descriptors and biological structures (both cell and organelle), which may provide additional or complementary insights and warrant systematic incorporation and evaluation [Tolonen et al., *bioRxiv*, 2025; van Bavel et al., *Bioinformatics*, 2023]. While specific 3D descriptor forms have demonstrated

unique strengths in certain biological contexts, their 2D counterparts may exhibit comparable performance and can be further developed and applied in scenarios where 2D imaging data are more accessible [Ramezani et al., *Nat. Methods*, 2025; Benkeder et al., *eLife*, 2025].

(2) The validation of cell morphology descriptors in identifying differential cell fates as well as gene expression faithfully establishes their power as a novel class of biosensors. This framework can be readily applied to existing cell morphology datasets across diverse multicellular developmental systems, including both the animal (*e.g.*, *Phallusia mammillata* [Biasuz et al., *bioRxiv*, 2025], *Ascidiella aspersa* [Biasuz et al., *bioRxiv*, 2025], *Drosophila melanogaster* [Stegmaier et al., *Dev. Cell*, 2016], *Platynereis dumerilii* [Vergara et al., *Cell*, 2021], *Pracentrotus lividus* [Villoutreix et al., *Sci. Rep.*, 2016], *Mus musculus* [Vianello, *bioRxiv*, 2020], *Danio rerio* [Olivier et al., *Science*, 2010]) and plant (*e.g.*, *Arabidopsis thaliana* [Kar et al., *PLoS Comput. Biol.*, 2022]) ones [Leggio et al., *Nat. Commun.*, 2019]. Such cross-system applications are expected to facilitate comparative studies of conserved developmental mechanisms across species as well as those unique to specific species. Given its non-invasive nature and compatibility with automated segmentation, this approach holds great promise for cell fate identification in both laboratory (routine monitoring of cell or organismal cultures) and clinical (rapid evaluation of patient-derived cell samples to assess health and disease states) environments, thereby replacing or complementing molecular assays that currently depend on large sample sizes and complex experimental procedures.

(3) Although the current cell morphology descriptors demonstrate strong performance in distinguishing major somatic cell fates (*incl.*, neuron, pharynx cells, muscle, intestine, skin), it remains unclear whether these or yet unexplored morphology descriptors can effectively discriminate additional cell fates (incl., germline cells, excretory cells, and unspecified progenitors whose descendants contribute to multiple somatic cell fates). Such fine-grained distinctions have traditionally been achieved through cell lineage tracing and gene expression profiling [Sulston et al., *Dev. Biol.*, 1977; Sulston et al., *Dev. Biol.*, 1983; Paczkó et al., *Commun. Biol.*, 2024], yet an equivalent morphology-based classifier remains to be established. Developing customized morphology descriptors tailored for specific fate distinctions could offer a unique advantage, particularly given their non-invasive nature, potential for high-throughput implementation in living systems, and straightforward indication of “morphogenesis”.

(4) Cell morphology may distinguish not only cell fates and gene expression but also diverse activities across scales [Barbier de Reuille et al., *eLife*, 2015; Guan et al., *Membranes*, 2024]. At cellular scales (*e.g.*, asymmetric division and intercalating movement tested in this study), cellular behaviors that have been reported with unique morphological features, such as cell adhesion [Hou et al., *Sci. Rep.*, 2019], cell stiffness [Chiang et al., *Biomaterials*, 2013], apoptosis [Chen et al., *Cell Death Dis.*, 2024], engulfment, migration, and so forth warrant further quantitative dissection through morphological characterization. At molecular scales, additional dimensions beyond conventional gene expression can be incorporated, such as trans-splicing [Yang et al., *Genome Res.*, 2017], chromatin accessibility [Zhao

et al., *Mol. Syst. Biol.*, 2021], metabolic profiling [Chen et al., *EMBO Rep.*, 2023], and microRNA landscapes [Xu et al., *Nat. Commun.*, 2024], all of which are closely linked to gene expression. While time-lapse imaging is typically restricted to monitoring one or a few molecular markers (*e.g.*, genes or proteins), whole-organism sequencing at specific developmental stages could significantly expand molecular coverage, transforming our 412-gene dataset into a genome-wide scale — albeit at the cost of cellular identity and temporal resolution. Altogether, integrating multi-scale datasets is expected to illuminate how physical and biological information are transmitted and converge to regulate development across scales. Beyond the co-differentiation analyses presented here, advanced data-mining strategies (*e.g.*, neural networks, deep learning, and other AI-based frameworks) may help uncover hidden correlations among features. Furthermore, theoretical modeling that bridges molecular dynamics and cellular behaviors centered on morphology will be essential for achieving a mechanistic understanding of the coupling between physical form and biological function.

Limitation of the study

Although our study statistically exposes the decoupled and coupled differentiation of 412 gene expression profiles and 12 cell morphology descriptors (Figure 3; Figure 4; Figure 5; Figure 6), these quantities occupy only a subset of the full underlying information within these two dimensions. On one side, the *C. elegans* genome is known to contain more than 20,000 protein-encoding genes [Spieth et al., *WormBook*, 2014] – in the future, sequencing data of both transcriptome and proteome could be utilized to reveal more comprehensive differentiation dynamics across genes on the order of tens of thousands [Grün et al., *Cell Rep.*, 2014; Tintori et al., *Dev. Cell*, 2016; Packer et al., *Science*, 2019; Ma et al., *Nat. Methods*, 2021; Large et al., *Science*, 2025]. On the other side, each 3D cell morphology composed of thousands to millions of point-cloud vertices could be subjected to dimension reduction in optional ways – in the future, the other morphology descriptors (*e.g.*, convexity, solidity, fractal dimension, compactness, lacunarity) as well as the implicit representation (*e.g.*, spherical harmonics descriptor, shape spectrum, Graph-based descriptors, extended Gaussian images, angular radial transform, Laplacian-Beltrami operator and machine learning) could be utilized to reveal more comprehensive differentiation dynamics capturing different aspects of cell morphologies, especially including those subtle, hard to notice, or difficult to describe [Zhang et al., *Funda Agao para a Cincia ea Tecnologia, Lisboa, Portugal, Tech. Rep. Technical Report, DecorAR (FCT POSC/EIA/59938/2004)*, 2007; Saghi et al., *Phys. Rev. B*, 2008; Kazmi et al., *2013 10th International Conference Computer Graphics, Imaging and Visualization*, 2013; Liu et al., *Sensors*, 2017; Benkeder et al., *eLife*, 2025].

What's more, despite that analyses of both natural and perturbed embryos support the coupling between expression and cell morphology to some extent, how they are coupled and the causality (if any) between them, as well as the underlying mechanisms, are still largely unknown. This is crucial for both gene expression and cell morphology – what is the reason accounting for their differentiation, decoupled

or coupled? What is the resultant physiological function? While the majority of Notch signaling studies paid attention to its role in gene expression differentiation, how it impacts cell positions, cell morphologies, and cell contacts in parallel was unclear before. Our successful identification of these functions (Figure 2; FigureS3; Figure S4) suggests that similar analyses should be extended to other gene expression differentiation events to build a more comprehensive understanding of their morphological consequences, not only those associated with Notch signaling.

RESOURCE AVAILABILITY

Lead contact

Further information and requests for resources and reagents should be directed to and will be fulfilled by the lead contact, Hongli Wang (hlwang@pku.edu.cn).

Materials availability

Data and code availability

ACKNOWLEDGMENTS

We are deeply grateful to Prof. Chao Tang, Prof. Qi Ouyang, Prof. Chunxiong Luo, Dr. Long Qian and all members of the Wang Lab for their insightful discussions and generous support. We also thank the anonymous reviewers and audience of the 25th International Worm Meeting (where G.G. presented this work in a plenary talk) for their valuable comments and suggestions. Gratitude is extended to Prof. Zhiyuan Li, Prof. Xiongfei Fu, Prof. Tiancheng Xu and Dr. Pengfei Xu for their valuable suggestions presented during Y.C.'s attendance of the poster seesion of various conferences. We acknowledge the use of ChatGPT (https://chat.openai.com/) to refine the academic tone and accuracy of language, including grammatical structures, punctuation and vocabulary. This work was financially supported by the Major Program of the National Natural Science Foundation of China (No. 12090051) and the National Key Research and Development Program of China (No. 2018YFA0900200). Computation is partially conducted on Y9000P 2024: (cpu) intel® Core™ i9-14900HX; (gpu) NVIDIA GeForce RTX 4070 Laptop GPU 8GB.

AUTHOR CONTRIBUTIONS

Conceptualization, G.G., Y.C., and H.W.; data curation, G.G. and Y.C.; formal analysis, G.G., Y.C., and H.W.; Funding acquisition, H.W.; investigation, G.G., Y.C., and H.W.; methodology, G.G., Y.C.; project administration, H.W.; resources, G.G., Y.C., and H.W.; software, G.G. and Y.C.; supervision, H.W.; validation, G.G., Y.C., and H.W.; visualization, G.G., Y.C., and H.W.; Writing – original draft, G.G., Y.C., and H.W.; writing – review & editing, G.G., Y.C., and H.W.

DECLARATION OF INTERESTS

The authors declare no competing interests.

STAR★METHODS

Detailed methods are provided in the online version of this paper and include the following:

- KEY RESOURCES TABLE
- RESOURCE AVAILABILITY
  - Lead contact
  - Materials availability
  - Data and code availability
- EXPERIMENTAL MODEL AND STUDY PARTICIPANT DETAILS
  - *C. elegans* culture and maintenance
- METHOD DETAILS
  - Representation of cell division asymmetry and cell intercalation depth
- QUANTIFICATION AND STATISTICAL ANALYSIS
  - Mathematical basis of 3D cell morphology descriptors

SUPPLEMENTAL INFORMATION

Supplemental information can be found alongside this paper.

DECLARATION OF GENERATIVE AI AND AI-ASSISTED TECHNOLOGIES

During the preparation of this work, the authors Guoye Guan and Yixuan Chen used ChatGPT [https://chatgpt.com] and deepseek [https://zaiwen.xueban.org.cn/; https://www.deepseek.com/] in order to polish the language of manuscript content. After using these tools, the authors reviewed and edited the content as needed and take full responsibility for the content of the publication.

REFERENCES

1. Alizadeh, E., Castle, J., Quirk, A., Taylor, C.D.L., Xu, W., and Prasad, A. (2020). Cellular morphological features are predictive markers of cancer cell state. Comput. Biol. Med. *126*, 104044. 10.1016/j.compbiomed.2020.104044.

2. Altun, Z.F., and Hall, D.H. (2009). Introduction to *C. elegans* anatomy. In WormAtlas. 10.3908/wormatlas.1.1.

3. Arata, Y., Takagi, H., Sako, Y., and Sawa, H. (2015). Power law relationship between cell cycle duration and cell volume in the early embryonic development of *Caenorhabditis elegans*. Front. Physiol. *5*, 529. 10.3389/fphys.2014.00529.

14. Asan, A., Raiders, S.A., and Priess, J.R. (2016). Morphogenesis of the *C. elegans* intestine involves axon guidance genes. PLoS Genet. *12*, e1005950. 10.1371/journal.pgen.1005950.

15. Azuma, Y., Okada, H., and Onami, S. (2023). Systematic analysis of cell morphodynamics in *C. elegans* early embryogenesis. Front. Bioinform. *3*, 1082531. 10.3389/fbinf.2023.1082531.

16. Azuma, Y., and Onami, S. (2014). Automatic cell identification in the unique system of invariant embryogenesis in *Caenorhabditis elegans*. Biomed. Eng. Lett. *4*, 328–337. 10.1007/s13534-014-0162-y.

17. Azuma, Y., and Onami, S. (2017). Biologically constrained optimization based cell membrane segmentation in *C. elegans* embryos. BMC Bioinformatics *18*, 307. 10.1186/s12859-017-1717-6.

18. Azuma, Y., Okada, H., and Onami, S. (2023). Systematic analysis of cell morphodynamics in *C. elegans* early embryogenesis. Front. Bioinform. *3*, 1082531. 10.3389/fbinf.2023.1082531.

19. Bao, Z., Murray, J.I., Boyle, T., Ooi, S.L., Sandel, M.J., and Waterston, R.H. (2006). Automated cell lineage tracing in *Caenorhabditis elegans*. Proc. Natl. Acad. Sci. U. S. A. *103*, 2707–2712. 10.1073/pnas.0511111103.

20. Barbier de Reuille, P., Routier-Kierzkowska, A.L., Kierzkowski, D., Bassel, G.W., Schüpbach, T., Tauriello, G., Bajpai, N., Strauss, S., Weber, A., Kiss, A., et al. (2015). MorphoGraphX: A platform for quantifying morphogenesis in 4D. eLife *4*, 05864. 10.7554/eLife.05864.

21. Benkeder, S., Dinh, S.M., Marchal, P., De Gea, P., Thoby-Brisson, M., Hubert, V., Hristovska, I., Pitollat, G., Combet, K., Cardoit, L., et al. (2025). MorphoCellSorter is an Andrews plot-based sorting approach to rank microglia according to their morphological features. eLife *13*, RP101630. 10.7554/eLife.101630.

22. Bennabi, I., Hansen, P., Merle, M., Pineau, J., Lopez-Delisle, L., Kolly, D., Duboule, D., Mayran, A., and Gregor, T. (2025). Size-dependent temporal decoupling of morphogenesis and transcriptional programs in pseudoembryos. Sci. Adv. *11*, eadv7790. 10.1126/sciadv.adv7790.

23. Bhaskar, D., Lee, D., Knútsdóttir, H., Tan, C., Zhang, M., Dean, P., Roskelley, C., and Edelstein-Keshet, L. (2019). A methodology for morphological feature extraction and unsupervised cell classification. bioRxiv 10.1101/623793.

24. Biasuz, K., Jammoul, H., Gallean, B., Asloudj, Y., Laussu, J., Lemaire, P., and Malandain, G. (2025). Automated cell naming reveals reproducible and variable features of ascidian embryogenesis. bioRxiv 10.1101/2025.10.13.681089.

25. Boyle, T.J., Bao, Z., Murray, J.I., Araya, C.L., and Waterston, R.H. (2006). AceTree: a tool for visual analysis of *Caenorhabditis elegans* embryogenesis. BMC Bioinformatics *7*, 275. 10.1186/1471-2105-

7-275.

16. Brenner, S. (1974). The genetics of *Caenorhabditis elegans*. Genetics *77*, 71–94. 10.1093/genetics/77.1.71.

17. *C. elegans* Sequencing Consortium. (1998). Genome sequence of the nematode *C. elegans*: a platform for investigating biology. Science *282*, 2012–2018. 10.1126/science.282.5396.2012.

18. Cao, J., Guan, G., Ho, V.W.S., Wong, M.-K., Chan, L.Y., Tang, C., Zhao, Z., and Yan, H. (2020). Establishment of a morphological atlas of the *Caenorhabditis elegans* embryo using deep-learning-based 4D segmentation. Nat. Commun. *11*, 6254. 10.1038/s41467-020-19863-x.

19. Cao, J., Hu, L., Guan, G., Li, L., Zhao, Z., Tang, C., and Yan, H. (2024). CShaperApp: Segmenting and analyzing cellular morphologies of the developing *Caenorhabditis elegans* embryo. Quant. Biol. *12*, 329–334. 10.1002/qub2.47.

20. Cedikova, M., Kripnerová, M., Dvorakova, J., Pitule, P., Grundmanova, M., Babuska, V., Mullerova, D., and Kuncova, J. (2016). Mitochondria in white, brown, and beige adipocytes. Stem Cells Int. *2016*, 6067349. 10.1155/2016/6067349.

21. Chen, D., Sarkar, S., Candia, J., Florczyk, S.J., Bodhak, S., Driscoll, M.K., Simon, C.G., Jr, Dunkers, J.P., and Losert, W. (2016). Machine learning based methodology to identify cell shape phenotypes associated with microenvironmental cues. Biomaterials *104*, 104–118. 10.1016/j.biomaterials.2016.06.040.

22. Chen, L., Ho, V.W.S., Wong, M.-K., Huang, X., Chan, L.-Y., Ng, H.C.K., Ren, X., Yan, H., and Zhao, Z. (2018). Establishment of signaling interactions with cellular resolution for every cell cycle of embryogenesis. Genetics *209*, 37–49. 10.1534/genetics.118.300820.

23. Chen, S., Su, X., Zhu, J., Xiao, L., Cong, Y., Yang, L., Du, Z., and Huang, X. (2023). Metabolic plasticity sustains the robustness of *Caenorhabditis elegans* embryogenesis. EMBO Rep. *24*, e57440. 10.15252/embr.202357440.

24. Chen, Y., Guan, G., Tang, L.-H., and Tang, C. (2025). Balancing reaction-diffusion network for cell polarization pattern with stability and asymmetry. eLife *13*, RP96421. 10.7554/eLife.96421.

25. Chen, Y., Li, X., Yang, M., and Liu, S.-B. (2024). Research progress on morphology and mechanism of programmed cell death. Cell Death Dis. *15*, 327. 10.1038/s41419-024-06712-8.

26. Chiang, M.Y., Yangben, Y., Lin, N.J., Zhong, J.L., and Yang, L. (2013). Relationships among cell morphology, intrinsic cell stiffness and cell-substrate interactions. Biomaterials *34*, 9754–9762. 10.1016/j.biomaterials.2013.09.014.

27. Chisholm, A.D., and Hardin, J. (2005). Epidermal morphogenesis. In: WormBook: The Online Review

of *C. elegans* Biology [Internet]. Pasadena (CA): WormBook; 2005-2018. https://www.ncbi.nlm.nih.gov/books/NBK19676/.

28. Cole, A.G., Hashimshony, T., Du, Z., and Yanai, I. (2024). Gene regulatory patterning codes in early cell fate specification of the *C. elegans* embryo. eLife *12*, RP87099. 10.7554/eLife.87099.

29. Cote, L.E., Sallee, M.D., Ng, R.K., Pickett, M.A., Magescas, J., and Feldman, J.L. (2025). Reciprocal E-cadherin signaling aligns apical surfaces between neighboring epithelial tissues to complete the *C. elegans* digestive tract. bioRxiv 10.1101/2025.10.06.680605.

30. Collinet, C., Rauzi, M., Lenne, P.F., and Lecuit, T. (2015). Local and tissue-scale forces drive oriented junction growth during tissue extension. Nat. Cell Biol. *17*, 1247–1258. 10.1038/ncb3226.

31. Dean, L. (2005). Blood Groups and Red Cell Antigens [Internet]. Bethesda (MD): National Center for Biotechnology Information (US); Chapter 1, Blood and the cells it contains. https://www.ncbi.nlm.nih.gov/books/NBK2263/.

32. Dibus, M., Joshi, O., and Ivaska, J. (2024). Novel tools to study cell-ECM interactions, cell adhesion dynamics and migration. Curr. Opin. Cell Biol. *88*, 102355. 10.1016/j.ceb.2024.102355.

33. Du, Z., Santella, A., He, F., Tiongson, M., and Bao, Z. (2014). De novo inference of systems-level mechanistic models of development from live-imaging-based phenotype analysis. Cell *156*, 359-372. 10.1016/j.cell.2013.11.046.

34. Du, Z., Santella, A., He, F., Shah, P.K., Kamikawa, Y., and Bao, Z. (2015). The regulatory landscape of lineage differentiation in a metazoan embryo. Dev. Cell *34*, 592–607. 10.1016/j.devcel.2015.07.014.

35. Farrell, J.A., Wang, Y., Riesenfeld, S.J., Shekhar, K., Regev, A., and Schier, A.F. (2018). Single-cell reconstruction of developmental trajectories during zebrafish embryogenesis. Science *360*, eaar3131. 10.1126/science.aar3131.

36. Fletcher, D.A., and Mullins, R.D. (2010). Cell mechanics and the cytoskeleton. Nature *463*, 485–492. 10.1038/nature08908.

37. Friedl, P., and Gilmour, D. (2009). Collective cell migration in morphogenesis, regeneration and cancer. Nat. Rev. Mol. Cell Biol. *10*, 445–457. 10.1038/nrm2720.

38. Fujii, Y., Koizumi, W.C., Imai, T., Yokobori, M., Matsuo, T., Oka, K., Hotta, K., and Okajima, T. (2021). Spatiotemporal dynamics of single cell stiffness in the early developing ascidian chordate embryo. Commun. Biol. *4*, 341. 10.1038/s42003-021-01869-w.

39. Goldstein, B. (1995). Cell contacts orient some cell division axes in the *Caenorhabditis elegans* embryo. J. Cell Biol. *129*, 1071-1080. 10.1083/jcb.129.4.1071.

40. Green, R.A., Khaliullin, R.N., Zhao, Z., Ochoa, S.D., Hendel, J.M., Chow, T.L., Moon, H., Biggs, R.J., Desai, A., and Oegema, K. (2024). Automated profiling of gene function during embryonic development. Cell *187*, 3141–3160.e23. 10.1016/j.cell.2024.04.012.

41. Greenwald, I., and Kovall, R. (2013). Notch signaling: genetics and structure. WormBook, ed. The *C. elegans* Research Community, WormBook, 10.1895/wormbook.1.10.2.

42. Grün, D., Kirchner, M., Thierfelder, N., Stoeckius, M., Selbach, M., and Rajewsky, N. (2014). Conservation of mRNA and protein expression during development of *C. elegans*. Cell Rep. *6*, 565–577. 10.1016/j.celrep.2014.01.001.

43. Guan, G., Chen, Y., Wang, H., Ouyang, Q., and Tang, C. (2024). Characterizing cellular physiological states with three-dimensional morphology descriptors for cell membranes. Membranes *14*, 137. 10.3390/membranes14060137.

44. Guan, G., Fang, M., Wong, M.-K., Ho, V.W.S., An, X., Tang, C., Huang, X., and Zhao, Z. (2020). Multilevel regulation of muscle-specific transcription factor *hlh-1* during *Caenorhabditis elegans* embryogenesis. Dev. Genes Evol. *230*, 265–278. 10.1007/s00427-020-00662-9.

45. Guan, G., Kuang, X., Tang, C., and Zhang, L. (2023). Comparison between phase-field model and coarse-grained model for characterizing cell-resolved morphological and mechanical properties in a multicellular system. Commun. Nonlinear Sci. Numer. Simul. *117,* 106966. 10.1016/j.cnsns.2022.106966.

46. Guan, G., Li, Z., Ma, Y., Ye, P., Cao, J., Wong, M.-K., Ho, V.W.S., Chan, L.Y., Yan, H., Tang, C., et al. (2025). Cell lineage-resolved embryonic morphological map reveals signaling associated with cell fate and size asymmetry. Nat. Commun. *16*, 3700. 10.1038/s41467-025-58878-0.

47. Guan, G., Wong, M.-K., Ho, V.W.S., An, X., Chan, L.-Y., Tian, B., Li, Z., Tang, L., Zhao, Z., and Tang, C. (2019). System-level quantification and phenotyping of early embryonic morphogenesis of *Caenorhabditis elegans*. bioRxiv 10.1101/776062.

48. Guan, G., Zhao, Z., and Tang, C. (2022). Delineating the mechanisms and design principles of *Caenorhabditis elegans* embryogenesis using *in toto* high-resolution imaging data and computational modeling. Comput. Struct. Biotechnol. J. *20*, 5500–5515. 10.1016/j.csbj.2022.08.024.

49. Hanahan, D., and Weinberg, R.A. (2011). Hallmarks of cancer: the next generation. Cell *144*, 646–674. 10.1016/j.cell.2011.02.013.

50. Haupt, A., and Minc, N. (2018). How cells sense their own shape - mechanisms to probe cell geometry and their implications in cellular organization and function. J. Cell Sci. *131*, jcs214015. 10.1242/jcs.214015.

51. Hayakawa, Y., and Oguchi, T. (2005). Evaluation of gravel sphericity and roundness based on surface-area measurement with a laser scanner. Comput. Geosci. *31*, 735–741. 10.1016/j.cageo.2005.01.004.

52. Heller, E., Kumar, K.V., Grill, S.W., and Fuchs, E. (2014). Forces generated by cell intercalation tow epidermal sheets in mammalian tissue morphogenesis. Dev. Cell *28*, 617–632. 10.1016/j.devcel.2014.02.011.

53. Hou, H.-S., Lee, K.-L., Wang, C.-H., Hsieh, T.-H., Sun, J.-J., Wei, P.-K., and Cheng, J.-Y. (2019). Simultaneous assessment of cell morphology and adhesion using aluminum nanoslit-based plasmonic biosensing chips. Sci. Rep. *9*, 7204. 10.1038/s41598-019-43442-w.

54. Huang, X.-T., Zhu, Y., Chan, L.H.L., Zhao, Z., and Yan, H. (2017). Inference of cellular level signaling networks using single-cell gene expression data in *Caenorhabditis elegans* reveals mechanisms of cell fate specification. Bioinformatics *33*, 1528–1535. 10.1093/bioinformatics/btw796.

55. Hunt-Newbury, R., Viveiros, R., Johnsen, R., Mah, A., Anastas, D., Fang, L., Halfnight, E., Lee, D., Lin, J., Lorch, A., et al. (2007). High-throughput *in vivo* analysis of gene expression in *Caenorhabditis elegans*. PLoS Biol. *5*, e237. 10.1371/journal.pbio.0050237.

56. Ichbiah, S., Delbary, F., McDougall, A., Dumollard, R., and Turlier, H. (2023). Embryo mechanics cartography: inference of 3D force atlases from fluorescence microscopy. Nat. Methods *20*, 1989–1999. 10.1038/s41592-023-02084-7.

57. Jankele, R., Jelier, R., and Gönczy, P. (2021). Physically asymmetric division of the *C. elegans* zygote ensures invariably successful embryogenesis. eLife *10*, e61714. 10.7554/eLife.61714.

58. Jelier, R., Kruger, A., Swoger, J., Zimmermann, T., and Lehner, B. (2016). Compensatory cell movements confer robustness to mechanical deformation during embryonic development. Cell Syst. *3*, 160–171. 10.1016/j.cels.2016.07.005.

59. Junyent, S., Meglicki, M., Vetter, R., Mandelbaum, R., King, C., Patel, E.M., Iwamoto-Stohl, L., Reynell, C., Chen, D.Y., Rubino, P., et al. (2024). The first two blastomeres contribute unequally to the human embryo. Cell *187*, 2838–2854.e17. 10.1016/j.cell.2024.04.029.

60. Kaletta, T., Schnabel, H., and Schnabel, R. (1997). Binary specification of the embryonic lineage in *Caenorhabditis elegans*. Nature *390*, 294–298. 10.1038/36869.

61. Kar, A., Petit, M., Refahi, Y., Cerutti, G., Godin, C., and Traas, J. (2022). Benchmarking of deep learning algorithms for 3D instance segmentation of confocal image datasets. PLoS Comput. Biol. *18*, e1009879. 10.1371/journal.pcbi.1009879.

62. Katzman, B., Tang, D., Santella, A., and Bao, Z. (2018). AceTree: a major update and case study in the long term maintenance of open-source scientific software. BMC Bioinformatics *19*, 121.

10.1186/s12859-018-2127-0.

63. Kazmi, I.K., You, L. and Zhang, J.J. (2013). A Survey of 2D and 3D Shape Descriptors. 2013 10th International Conference Computer Graphics, Imaging and Visualization, Los Alamitos, CA, USA, pp. 1-10. 10.1109/CGIV.2013.11.

64. Khan, Z., Wang, Y.C., Wieschaus, E.F., and Kaschube, M. (2014). Quantitative 4D analyses of epithelial folding during *Drosophila* gastrulation. Development *141*, 2895–2900. 10.1242/dev.107730.

65. Khatri, D., Negi, P., and Athale, C.A. (2025). Classification of first embryonic division stages of multiple *Caenorhabditis* species by deep learning. npj Syst. Biol. Appl. *11*, 97. 10.1038/s41540-025-00566-2.

66. Large, C.R.L., Khanal, R., Hillier, L., Huynh, C., Kubo, C., Kim, J., Waterston, R.H., and Murray, J.I. (2025). Lineage-resolved analysis of embryonic gene expression evolution in *C. elegans* and *C. briggsae*. Science *388*, eadu8249. 10.1126/science.adu8249.

67. Laznovsky, J., Kavkova, M., Helena Reis, A., Robovska-Havelkova, P., Maia, L.A., Krivanek, J., Zikmund, T., Kaiser, J., Buchtova, M., and Harnos, J. (2024). Unveiling vertebrate development dynamics in frog Xenopus laevis using micro-CT imaging. Gigascience *13*, giae037.10.1093/gigascience/giae037.

68. Le Clainche, C., and Carlier, M.F. (2008). Regulation of actin assembly associated with protrusion and adhesion in cell migration. Physiol. Rev. *88*, 489–513. 10.1152/physrev.00021.2007.

69. Lee, H., and Chen, Y.-P.P. (2014). Cell morphology based classification for red cells in blood smear images. Pattern Recogn. Lett. *49*, 155–161. 10.1016/j.patrec.2014.06.010.

70. Lee, J.-Y., Marston, D.J., Walston, T., Hardin, J., Halberstadt, A., and Goldstein, B. (2006). Wnt/Frizzled signaling controls *C. elegans* gastrulation by activating actomyosin contractility. Curr. Biol. *16*, 1986–1997. 10.1016/j.cub.2006.08.090.

71. Leggio, B., Laussu, J., Carlier, A., Godin, C., Lemaire, P., and Faure, E. (2019). *MorphoNet*: an interactive online morphological browser to explore complex multi-scale data. Nat. Commun. *10*, 2812. 10.1038/s41467-019-10668-1.

72. Leung, B., Hermann, G.J., and Priess, J.R. (1999). Organogenesis of the *Caenorhabditis elegans* intestine. Dev. Biol. *216*, 114–134. 10.1006/dbio.1999.9471.

73. Li, X., Zhao, Z., Xu, W., Fan, R., Xiao, L., Ma, X., and Du, Z. (2019). Systems properties and spatiotemporal regulaticon of cell position variability during embryogenesis. Cell Rep. *26*, 313–321.e7. 10.1016/j.celrep.2018.12.052.

74. Lim, H.Y.G., and Plachta, N. (2021). Cytoskeletal control of early mammalian development. Nat. Rev.

Mol. Cell Biol. *22*, 548–562. 10.1038/s41580-021-00363-9.

75. Liu, J., and Murray, J.I. (2023). Mechanisms of lineage specification in *Caenorhabditis elegans*. Genetics *225*, iyad174. 10.1093/genetics/iyad174.

76. Liu, Z., Zhao, C., Wu, X., and Chen, W. (2017). An effective 3D shape descriptor for object recognition with RGB-D sensors. Sensors *17*, 451. 10.3390/s17030451.

77. Liu, Z. (2025). venn diagram. (https://ww2.mathworks.cn/matlabcentral/fileexchange/116760-venn-diagram), MATLAB Central File Exchange.

78. Luxenburg, C., and Zaidel-Bar, R. (2019). From cell shape to cell fate via the cytoskeleton - Insights from the epidermis. Exp. Cell Res. *378*, 232–237. 10.1016/j.yexcr.2019.03.016.

79. Lyczak, R., Gomes, J.E., and Bowerman, B. (2002). Heads or tails: cell polarity and axis formation in the early *Caenorhabditis elegans* embryo. Dev. Cell *3*, 157–166. 10.1016/s1534-5807(02)00226-5.

80. Ma, X., Zhao, Z., Xiao, L., Xu, W., Kou, Y., Zhang, Y., Wu, G., Wang, Y., and Du, Z. (2021). A 4D single-cell protein atlas of transcription factors delineates spatiotemporal patterning during embryogenesis. Nat. Methods *18*, 893–902. 10.1038/s41592-021-01216-1.

81. Maduro, M.F. (2017). Gut development in *C. elegans*. Semin. Cell Dev. Biol. *66*, 3–11. 10.1016/j.semcdb.2017.01.001.

82. Mello, C.C., Draper, B.W., and Priess, J.R. (1994). The maternal genes *apx-1* and *glp-1* and establishment of dorsal-ventral polarity in the early *C. elegans* embryo. Cell *77*, 95–106. 10.1016/0092-8674(94)90238-0.

83. Mestek Boukhibar, L., and Barkoulas, M. (2016). The developmental genetics of biological robustness. Ann. Bot. *117*, 699–707. 10.1093/aob/mcv128.

84. Mickey, K.M., Mello, C.C., Montgomery, M.K., Fire, A., and Priess, J.R. (1996). An inductive interaction in 4-cell stage *C. elegans* embryos involves APX-1 expression in the signalling cell. Development *122*, 1791–1798. 10.1242/dev.122.6.1791.

85. Moore, J.L., Du, Z., and Bao, Z. (2013). Systematic quantification of developmental phenotypes at single-cell resolution during embryogenesis. Development *140*, 3266–3274. 10.1242/dev.096040.

86. Moris, N., Anlas, K., van den Brink, S.C., Alemany, A., Schröder, J., Ghimire, S., Balayo, T., van Oudenaarden, A., and Martinez Arias, A. (2020). An in vitro model of early anteroposterior organization during human development. Nature *582*, 410–415. 10.1038/s41586-020-2383-9.

87. Murray, J.I., Bao, Z., Boyle, T. J., and Waterston, R.H. (2006). The lineaging of fluorescently-labeled *Caenorhabditis elegans* embryos with StarryNite and AceTree. Nat. Protoc. *1*, 1468–1476. 10.1038/nprot.2006.222.

88. Murray, J.I., Bao, Z., Boyle, T.J., Boeck, M.E., Mericle, B.L., Nicholas, T.J., Zhao, Z., Sandel, M.J., and Waterston, R.H. (2008). Automated analysis of embryonic gene expression with cellular resolution in *C. elegans*. Nat. Methods *5*, 703–709. 10.1038/nmeth.1228.

89. Murray, J.I. (2018). Systems biology of embryonic development: Prospects for a complete understanding of the *Caenorhabditis elegans* embryo. Wiley Interdiscip. Rev. Dev. Biol. *7*, e314. 10.1002/wdev.314.

90. Murray, J.I., Boyle, T.J., Preston, E., Vafeados, D., Mericle, B., Weisdepp, P., Zhao, Z., Bao, Z., Boeck, M., and Waterston, W.H. (2012). Multidimensional regulation of gene expression in the *C. elegans* embryo. Genome Res. *22*, 1282–1294. 10.1101/gr.131920.111.

91. Nance, J., Lee, J.Y., and Goldstein, B. (2005). Gastrulation in *C. elegans*. WormBook. 1–13. 10.1895/wormbook.1.23.1.

92. Olivier, N., Luengo-Oroz, M.A., Duloquin, L., Faure, E., Savy, T., Veilleux, I., Solinas, X., Débarre, D., Bourgine, P., Santos, A., et al. (2010). Cell lineage reconstruction of early zebrafish embryos using label-free nonlinear microscopy. Science *329*, 967–971. 10.1126/science.1189428.

93. Packer, J.S., Zhu, Q., Huynh, C., Sivaramakrishnan, P., Preston, E., Dueck, H., Stefanik, D., Tan, K., Trapnell, C., Kim, J., et al. (2019). A lineage-resolved molecular atlas of *C. elegans* embryogenesis at single-cell resolution. Science *365*, eaax1971. 10.1126/science.aax1971.

94. Paczkó, M., Vörös, D., Szabó, P., Jékely, G., Szathmáry, F., and Szilágyi, A. (2024). A neural network-based model framework for cell-fate decisions and development. Commun. Biol. *7*, 323. 10.1038/s42003-024-05985-1.

95. Pasternak, T., Haser, T., Falk, T., Ronneberger, O., Palme, K., and Otten, L. (2017). A 3D digital atlas of the *Nicotiana tabacum* root tip and its use to investigate changes in the root apical meristem induced by the *Agrobacterium 6b* oncogene. Plant J. *92*, 31–42. 10.1111/tpj.13631.

96. Pimpale, L.G., Middelkoop, T.C., Mietke, A., and Grill, S.W. (2020). Cell lineage-dependent chiral actomyosin flows drive cellular rearrangements in early *Caenorhabditis elegans* development. eLife *9*, e54930. 10.7554/eLife.54930.

97. Pineau, J., Wong-Ng, J., Mayranm, A., Lopez-Delisle, L., Osteil, P., Shoushtarizadeh, A., Duboule, D., Gobaa, S., and Gregor, T. (2025). Fine-tuning mechanical constraints reveals uncoupled patterning and gene expression programs in murine gastruloids. Development *152*, dev204711. 10.1242/dev.204711.

98. Priess, J. (2005). Notch signaling in the *C. elegans* embryo. WormBook 1–16. 10.1895/wormbook.1.4.1.

99. Qiu, X., Zhu, D.Y., Lu, Y., Yao, J., Jing, Z., Min, K.H., Cheng, M., Pan, H., Zuo, L., King, S., et al.

(2024). Spatiotemporal modeling of molecular holograms. Cell *187*, 7351–7373.e61. 10.1016/j.cell.2024.10.011.

100. Ramezani, M., Weisbart, E., Bauman, J., Singh, A., Yong, J., Lozada, M., Way, G.P., Kavar, S.L., Diaz, C., Leardini, E., et al. (2025). A genome-wide atlas of human cell morphology. Nat. Methods *22*, 621–633. 10.1038/s41592-024-02537-7.

101. Richards, J.L., Zacharias, A.L., Walton, T., Burdick, J.T., and Murray, J.I. (2013). A quantitative model of normal *Caenorhabditis elegans* embryogenesis and its disruption after stress. Dev. Biol. *374*, 12–23. 10.1016/j.ydbio.2012.11.034.

102. Ridley, A.J., Schwartz, M.A., Burridge, K., Firtel, R.A., Ginsberg, M.H., Borisy, G., Parsons, J.T., and Horwitz, A.R. (2003). Cell migration: integrating signals from front to back. Science *302*, 1704–1709. 10.1126/science.1092053.

103. Rose, L., and Gönczy, P. (2014). Polarity establishment, asymmetric division and segregation of fate determinants in early *C. elegans* embryos. WormBook. 1–43. 10.1895/wormbook.1.30.2.

104. Rossant, J., and Tam, P.P.L. (2022). Early human embryonic development: Blastocyst formation to gastrulation. Dev. Cell *57*, 152–165. 10.1016/j.devcel.2021.12.022.

105. Saghi, Z., Xu, X., and Möbus, G. (2008). Three-dimensional metrology and fractal analysis of dendritic nanostructures. Phys. Rev. B *78*, 205428. 10.1103/PhysRevB.78.205428.

106. Santella, A., Kovacevic, I., Herndon, L.A., Hall, D.H., Du, Z., and Bao, Z. (2016). Digital development: a database of cell lineage differentiation in *C. elegans* with lineage phenotypes, cell-specific gene functions and a multiscale model. Nucleic Acids Res. *44*, D781–D785. 10.1093/nar/gkv1119.

107. Sato, M., Akashi, H., Sakamoto, Y., Matsunaga, S., and Tsuji, H. (2021). Whole-tissue three-dimensional imaging of rice at single-cell resolution. Int. J. Mol. Sci. *23*, 40. 10.3390/ijms23010040.

108. Schnabel, R., Hutter, H., Moerman, D., and Schnabel, H. (1997). Assessing normal embryogenesis in *Caenorhabditis elegans* using a 4D microscope: variability of development and regional specification. Dev. Biol. *184*, 234–265. 10.1006/dbio.1997.8509.

109. Sladitschek, H.L., Fiuza, U.M., Pavlinic, D., Benes, V., Hufnagel, L., and Neveu, P.A. (2020). MorphoSeq: Full single-cell transcriptome dynamics up to gastrulation in a chordate. Cell *181*, 922–935.e21. 10.1016/j.cell.2020.03.055.

110. Spieth, J., Lawson, D., Davis, P., Williams, G., and Howe, K. (2014). Overview of gene structure in *C. elegans*. In: WormBook: The Online Review of *C. elegans* Biology [Internet], J. Hodgkin, ed. (Pasadena, CA). 10.1895/wormbook.1.65.2.

111. Stegmaier, J., Amat, F., Lemon, W.C., McDole, K., Wan, Y., Teodoro, G., Mikut, R., and Keller, P.J. (2016). Real-time three-dimensional cell segmentation in large-scale microscopy data of developing embryos. Dev. Cell *36*, 225–240. 10.1016/j.devcel.2015.12.028.

112. Sugioka, K., and Bowerman, B. (2018). Combinatorial contact cues specify cell division orientation by directing cortical myosin flows. Dev. Cell *46*, 257–270.e5. 10.1016/j.devcel.2018.06.020.

113. Sulston J.E. (1976). Post-embryonic development in the ventral cord of *Caenorhabditis elegans*. Philos. Trans. R. Soc. Lond. B Biol. Sci. *275*, 287–297. 10.1098/rstb.1976.0084.

114. Sulston, J.E., and Horvitz, H.R. (1977). Post-embryonic cell lineages of the nematode, *Caenorhabditis elegans*. Dev. Biol. *56*, 110–156. 10.1016/0012-1606(77)90158-0.

115. Sulston, J.E., Schierenberg, E., White, J.G., and Thomson, J.N. (1983). The embryonic cell lineage of the nematode *Caenorhabditis elegans*. Dev. Biol. *100*, 64–119. 10.1016/0012-1606(83)90201-4.

116. Thiels, W., Smeets, B., Cuvelier, M., Caroti, F., and Jelier, R. (2021). spheresDT/Mpacts-PiCS: cell tracking and shape retrieval in membrane-labeled embryos. Bioinformatics *37*, 4851–4856. 10.1093/bioinformatics/btab557.

117. Tian, B., Guan, G., Tang, L.-H., and Tang, C. (2020). Why and how the nematode's early embryogenesis can be precise and robust: a mechanical perspective. Phys. Biol. *17*, 026001. 10.1088/1478-3975/ab6356.

118. Tintori, C.S., Osborne Nishimura, E., Golden, P., Lieb, J.D., and Goldstein, B. (2016). A transcriptional lineage of the early *C. elegans* embryo. Dev. Cell *38*, 430–444. 10.1016/j.devcel.2016.07.025.

119. Tolonen, M., Xu, Z., Beker, O., Kapoor, V., Dumitrascu, B., and Sedzinski, J. (2025). Single-cell morphodynamics predict cell fate decisions during mucociliary epithelial differentiation. bioRxiv 10.1101/2025.09.17.676780.

120. Truernit, E., Bauby, H., Dubreucq, B., Grandjean, O., Runions, J., Barthélémy, J., and Palauqui, J.-C. (2008). High-resolution whole-mount imaging of three-dimensional tissue organization and gene expression enables the study of phloem development and structure in *Arabidopsis*. Plant Cell *20*, 1494–1503. 10.1105/tpc.107.056069.

121. Uriu, K., and Morelli, L.G. (2023). Orchestration of tissue shape changes and gene expression patterns in development. Semin. Cell Dev. Biol. *147*, 24–33. 10.1016/j.semcdb.2022.12.009.

122. Vadori, V., Peruffo, A., Graïc, J.-M., Finos, L., and Grisan, E. (2024). Automated classification of cell shapes: a comparative evaluation of morphology descriptors. arXiv 10.48550/arXiv.2411.00561.

123. Vanslambrouck, M., Thiels, W., Vangheel, J., van Bavel, C., Smeets, B., and Jelier, B. (2024).

Image-based force inference by biomechanical simulation. PLoS Comput. Biol. *20*, e1012629. 10.1371/journal.pcbi.1012629.

124. van Bavel, C., Thiels, W., and Jelier, R. (2023). Cell shape characterization, alignment, and comparison using FlowShape. Bioinformatics *39*, btad383. 10.1093/bioinformatics/btad383.

125. Villoutreix, P., Delile, J., Rizzi, B., Duloquin, L., Savy, T., Bourgine, P., Doursat, R., and Peyriéras, N. (2016). An integrated modelling framework from cells to organism based on a cohort of digital embryos. Sci. Rep. *6*, 37438. 10.1038/srep37438.

126. Vergara, H.M., Pape, C., Meechan, K.I., Zinchenko, V., Genoud, C., Wanner, A.A., Mutemi, K.N., Titze, B., Templin, R.M., Bertucci, P.Y., et al. (2021). Whole-body integration of gene expression and single-cell morphology. Cell *184*, 4819–4837.e22. 10.1016/j.cell.2021.07.017.

127. Vianello, S. (2020). Exploring and illustrating the mouse embryo: virtual objects to think and create with. bioRxiv 10.1101/2020.11.23.393991.

128. Waddington, C.H. (1957). The Strategy of the Genes (1st ed.). Routledge. 10.4324/9781315765471.

129. Walck-Shannon, E., and Hardin, J. (2014). Cell intercalation from top to bottom. Nat. Rev. Mol. Cell Biol. *15*, 34–48. 10.1038/nrm3723.

130. Wilson, L., and Huang, T.C. (1979). The influence of shape on the atmospheric settling velocity of volcanic ash particles. Earth Planet. Sci. Lett. *44*, 311–324. 10.1016/0012-821x(79)90179-1.

131. Wu, D., Yamada, K.M., and Wang, S. (2023). Tissue morphogenesis through dynamic cell and matrix interactions. Annu. Rev. Cell Dev. Biol. *39*, 123–144. 10.1146/annurev-cellbio-020223-031019.

132. Xiao, L., Fan, D., Qi, H., Cong, Y., and Du, Z. (2022). Defect-buffering cellular plasticity increases robustness of metazoan embryogenesis. Cell Syst. *13*, 615–630.e9. 10.1016/j.cels.2022.07.001.

133. Xie, P., Shen, J., Yang, Y., Wang, X., Liu, W., Cao, H., Zheng , Y., Wu, C., Mao, G., Chen, L., et al. (2025). Digital reconstruction of full embryos during early mouse organogenesis. Cell *188*, 4754–4772.e18. 10.1016/j.cell.2025.05.035.

134. Xiong, R., Su, Y., Yao, M., Liu, Z., Lu, J., Chen, Y.-C., and Ao., P. (2025). Quantitative resolution of cell fate in the early embryogenesis of *Caenorhabditis elegans*. Genetics *230*, iyaf095. 10.1093/genetics/iyaf095.

135. Xiong, R., and Sugioka, K. (2020). Improved 3D cellular morphometry of *Caenorhabditis elegans* embryos using a refractive index matching medium. PLoS One *15*, e0238955. 10.1371/journal.pone.0238955.

136. Xu, W., Liu, J., Qi, H., Si, R., Zhao, Z., Tao, Z., Bai, Y., Hu, S., Sun, X., Cong, Y., et al. (2024). A lineage-resolved cartography of microRNA promoter activity in *C. elegans* empowers multidimensional developmental analysis. Nat. Commun. *15*, 2783. 10.1038/s41467-024-47055-4.

137. Yamamoto, K., Ichbiah, S., Perez, M., Borrego-Pinto, J., Delbary, F., Goehring, N., Turlier, H., and Charras, G. (2025). Spatiotemporal mapping of the contractile and adhesive forces sculpting early *C. elegans* embryos. bioRxiv 10.1101/2023.03.07.531437.

138. Yang, Y.-F., Zhang, X., Ma, X., Zhao, T., Sun, Q., Huan, Q., Wu, S., Du, Z., and Qian, W. (2017). *Trans*-splicing enhances translational efficiency in *C. elegans*. Genome Res. *27*, 1525–1535. 10.1101/gr.202150.115.

139. Yu, H., Lim, K.P., Xiong, S., Tan, L.P., and Shim, W. (2013). Functional morphometric analysis in cellular behaviors: shape and size matter. Adv. Healthc. Mater. *2*, 1188–1197. 10.1002/adhm.201300053.

140. Zacharias, A.L., Walton, T., Preston, E., and Murray, J.I. (2015). Quantitative differences in nuclear β-catenin and TCF pattern embryonic cells in *C. elegans*. PLoS Genet. *11*, e1005585. 10.1371/journal.pgen.1005585.

141. Zhang, L., Da Fonseca, M. J., Ferreira, A., and e Recuperaçao, C. R. A. (2007). Survey on 3D shape descriptors. Funda Agao para a Cincia ea Tecnologia, Lisboa, Portugal, Tech. Rep. Technical Report, DecorAR (FCT POSC/EIA/59938/2004), 3.

142. Zhao, Z., Fan, R., Xu, W., Kou, Y., Wang, Y., Ma, X., and Du, Z. (2021). Single-cell dynamics of chromatin activity during cell lineage differentiation in *Caenorhabditis elegans* embryos. Mol. Syst. Biol. *17*, e10075. 10.15252/msb.202010075.

STAR★METHODS

KEY RESOURCES TABLE

RESOURCE AVAILABILITY

Lead contact

Further information and requests for resources and reagents should be directed to the lead contact, Hongli Wang (hlwang@pku.edu.cn).

Materials availability

Data and code availability

·All resource data (Supplementary Data 1-4) are available on [https://www.dropbox.com/scl/fo/ynjioma2mfin454vyedwi/AMhusiAMIKter1YR9epx7c4?rlkey=15oji0q3w0c44aghy1afmu3wj&st=gvdsnu9m&dl=0].

EXPERIMENTAL MODEL AND STUDY PARTICIPANT DETAILS

- *C. elegans* culture and maintenance

No new *C. elegans* were cultured or maintained for this study. All raw data originates from the authors' experimental papers [Cao et al., *Nat. Commun.*, 2020; Guan et al., *Nat. Commun.*, 2025], where experimental details are fully described.

QUANTIFICATION AND STATISTICAL ANALYSIS

- Mathematical basis of 3D cell morphology descriptors

LINEAGE WITH CELL MORPHOLOGY AND GENE EXPRESSION

METHOD DETAILS

- Representation of cell division asymmetry and cell intercalation depth

1. Cell Division

To model the morphology during cell division, we assume cells to be perfect spheres with nuclei positioned at their centers. Consequently, a mother cell poised for division is represented by the overlap of two such spheres. We denote the radius of the larger cell (Daughter1) as r_1 and that of the smaller cell (Daughter2) as r_2. The distance between the two nuclei is fixed at L, and the distance between the overlapping parts of the two daughter cells is d, where L and d are quantified as constants. According to the schematic diagram of the maximum cross-section for a splitting mother cell shown in Figure S1C, the horizontal distance from the center of Daughter1 to the vertical plane delimiting the intersection region is given by d_1, while that of Daughter2 is given by d_2. Moreover, h represents the vertical height of the spherical cap formed at the intersection interface. The geometric relationship of the aforesaid parameters is given by:

$$\begin{cases} r_2 = L + d - r_1 \\ L = d_1 + d_2 \\ r_1^2 - d_1^2 = r_2^2 - d_2^2 \end{cases} \tag{1}$$

thus d_1 and d_2 can be reduced to

$$\begin{cases} d_1 = \dfrac{2Lr_1 + 2dr_1 - 2Ld - d^2}{2L} \\ d_2 = \dfrac{2L^2 + 2Ld - 2Lr_1 + d^2 - 2r_1 d}{2L} \end{cases} \tag{2}$$

To calculate the 12 3D morphology descriptors, some basic parameters, (*i.e.* volume V, surface area S, the representative axes of the oriented bounding box (OBB)) need to be quantified in advance (Figure 1A):

$$\begin{aligned} V &= \frac{\pi}{3}[(2r_1 - d)(r_1 + d)^2 + (2r_2 - d_2)(r_2 + d_2)^2] \\ &= \frac{\pi}{12L}(2L + d)^2(4L^2 + 8Ld - 12Lr_1 + 3d^2 - 12dr_1 + 12r_1^2) \end{aligned} \tag{3}$$

$$S = 2\pi[r_1(r_1 + d_1) + r_2(r_2 + d_2)] = \frac{\pi}{L}(2L + d)(2L^2 + 3Ld - 4Lr_1 + d^2 - 4dr_1 + 4r_1^2) \quad (4)$$

$$a = r_1 + r_2 + L = 2L + d \quad (5)$$

$$b = c = 2r_1 \quad (6)$$

Then, substituting the formula given in Figure 1A [Guan et al., *Membranes*, 2024], the 12 morphology descriptors are presented by the following equation:

$$M_{\text{General Sphericity}} = \frac{\sqrt[3]{36\pi V^2}}{S} = \frac{\sqrt[3]{2L(2L + d)(4L^2 + 8Ld - 12Lr_1 + 3d^2 - 12dr_1 + 12r_1^2)^2}}{2(2L^2 + 3Ld - 4Lr_1 + d^2 - 4dr_1 + 4r_1^2)} \quad (7)$$

$$M_{\text{Diameter Sphericity}} = \frac{\sqrt[3]{\frac{6V}{\pi}}}{a} = \sqrt[3]{\frac{4L^2 + 8Ld - 12Lr_1 + 3d^2 - 12dr_1 + 12r_1^2}{2L(2L + d)}} \quad (8)$$

$$M_{\text{Intercept Sphericity}} = \sqrt[3]{\frac{bc}{a^2}} = \sqrt[3]{\frac{4r_1^2}{(2L + d)^2}} \quad (9)$$

$$M_{\text{Maximum Projection Sphericity}} = \sqrt[3]{\frac{c^2}{ab}} = \sqrt[3]{\frac{2r_1}{2L + d}} \quad (10)$$

$$M_{\text{Hayakawa Roundness}} = \frac{V}{S\sqrt[3]{abc}} = \frac{4L^2 + 8Ld - 12Lr_1 + 3d^2 - 12dr_1 - 12r_1^2}{24(2L^2 + 3Ld - 4Lr_1 + d^2 - 4dr_1 + 4r_1^2)} \sqrt[3]{\frac{2(2L + d)^2}{r_1^2}} \quad (11)$$

$M_{\text{Spreading Index}}$ (Equation unshown, checkable in our matlab code)

$$M_{\text{Elongation Ratio}} = \frac{a}{b} = \frac{2L + d}{2r_1} \quad (12)$$

$$M_{\text{Pivotability Index}} = 1 \quad (13)$$

$$M_{\text{Wilson Flatness Index}} = \frac{c}{a} = \frac{2r_1}{2L + d} \quad (14)$$

$$M_{\text{Hayakawa Flatness Ratio}} = \frac{a + b}{2c} = \frac{2L + d + 2r_1}{4r_1} \quad (15)$$

$$M_{\text{Huang Shape Factor}} = \frac{b + c}{2a} = \frac{2r_1}{2L + d} \quad (16)$$

$$M_{\text{Corey Shape Factor}} = \frac{c}{\sqrt{ab}} = \frac{\sqrt{2}r_1}{\sqrt{r_1(2L + d)}} \quad (17)$$

We further verified whether the morphology descriptors are correlated with the volume or surface area asymmetry during cell division. According to the definitions of volume asymmetry Δ_V and surface area asymmetry Δ_S:

$$\Delta_V = \frac{|V_a - V_p|}{V_a + V_p} = \frac{r_1^3 - r_2^3}{r_1^3 + r_2^3} = \frac{2r_1^3}{(L + d - r_1)^3 + r_1^3} - 1 \quad (18)$$

$$\Delta_S = \frac{|S_a - S_p|}{S_a + S_p} = \frac{r_1^2 - r_2^2}{r_1^2 + r_2^2} = \frac{2r_1^2}{(L + d - r_1)^2 + r_1^2} - 1 \quad (19)$$

According to the chain rule, the correlatio can be determined by the sign of the derivative:

$$\frac{\mathrm{d}M_i}{\mathrm{d}\Delta_j} = \frac{\mathrm{d}M_i}{\mathrm{d}r_1} \times \frac{\mathrm{d}r_1}{\mathrm{d}\Delta_j} \tag{20}$$

where M_i represents any morphology descriptor, and Δ_j are Δ_V or Δ_S. Substituting specific morphology descriptor yields:

(1) General Sphericity (monotonicity: increasing)

$$\frac{\mathrm{d}\left(M_{\text{General Sphericity}}\right)}{\mathrm{d}\Delta_V} = \frac{[(L+d-r_1)^3 + r_1^3]^2(2r_1-d)(2L+d-2r_1)(2r_1-L-d)}{3r_1^2(L+d)(L+d-r_1)^2(2L^2+3Ld-4Lr_1+d^2-4dr_1+4r_1^2)^2} \times \sqrt[3]{\frac{2L(2L+d)}{4L^2+8Ld-12Lr_1+3d^2-12dr_1+12r_1^2}} \tag{21}$$

Given the constraint $d < 2r_2 < 2\sqrt{r_1^2+r_2^2-r_1r_2} < 2r_1$, the denominator term:

$$4L^2+8Ld-12Lr_1+3d^2-12dr_1+12r_1^2 = 4(r_1^2+r_2^2-r_1r_2)-d^2 > 0 \tag{22}$$

holds universally. Since all multiplicative terms in $\frac{d\left(M_{\text{General Sphericity}}\right)}{d\Delta_V}$ are positive under this contraints, we have $\frac{\mathrm{d}\left(M_{\text{General Sphericity}}\right)}{\mathrm{d}\Delta_V} > 0$

Thus, General Sphericity exhibits a positive correlation with volume asymmetry. Similarly,

$$\frac{\mathrm{d}\left(M_{\text{General Sphericity}}\right)}{\mathrm{d}\Delta_S} = \frac{(2r_1-d)(2L+d-2r_1)(2r_1-L-d)(L^2+2Ld-2Lr_1+d^2-2dr_1+2r_1^2)^2}{2r_1(L+d)(L+d-r_1)(2L^2+3Ld-4Lr_1+d^2-4dr_1+4r_1^2)^2} \times \sqrt[3]{\frac{2L(2L+d)}{4L^2+8Ld-12Lr_1+3d^2-12dr_1+12r_1^2}} > 0 \tag{23}$$

This confirms that General Sphericity is positively correlated with surface area asymmetry.

(2) Diameter Sphericity (monotonicity: increasing)

$$\frac{\mathrm{d}\left(M_{\text{Diameter Sphericity}}\right)}{\mathrm{d}\Delta_V} = \frac{(2r_1-L-d)[(L+d-r_1)^3+r_1^3]^2}{3r_1^2(L+d)(L+d-r_1)^2} \times \sqrt[3]{\frac{4}{L(2L+d)(4L^2+8Ld-12Lr_1+3d^2-12dr_1+12r_1^2)^2}} > 0 \tag{24}$$

$$\frac{\mathrm{d}\left(M_{\text{Diameter Sphericity}}\right)}{\mathrm{d}\Delta_S} = \frac{(2r_1-L-d)(L^2+2Ld-2Lr_1+d^2-2dr_1+2r_1^2)^2}{2r_1(L+d)(L+d-r_1)} \times \sqrt[3]{\frac{4}{L(2L+d)(4L^2+8Ld-12Lr_1+3d^2-12dr_1+12r_1^2)^2}} > 0 \tag{25}$$

Diameter Sphericity exhibits a positive correlation with both volume and surface area asymmetry.

(3) Intercept Sphericity (monotonicity: increasing)

$$\frac{\mathrm{d}\left(M_{\text{Intercept Sphericity}}\right)}{\mathrm{d}\Delta_V} = \frac{[(L+d-r_1)^3+r_1^3]^2}{9(L+d)(L+d-r_1)^2} \times \sqrt[3]{\frac{4}{r_1^7(2L+d)^2}} > 0 \tag{26}$$

$$\frac{\mathrm{d}\left(M_{\text{Intercept Sphericity}}\right)}{\mathrm{d}\Delta_S} = \frac{(L^2+2Ld-2Lr_1+d^2-2dr_1+2r_1^2)^2}{6(L+d)(L+d-r_1)} \times \sqrt[3]{\frac{4}{r_1^4(2L+d)^2}} > 0 \quad (27)$$

Intercept Sphericity exhibits a positive correlation with both volume and surface area asymmetry.

(4) Maximum Projection Sphericity (monotonicity: increasing)

$$\frac{\mathrm{d}\left(M_{\text{Maximum Projection Sphericity}}\right)}{\mathrm{d}\Delta_V} = \frac{[(L+d-r_1)^3+r_1^3]^2}{18(L+d)(L+d-r_1)^2} \times \sqrt[3]{\frac{2}{r_1^8(2L+d)}} > 0 \quad (28)$$

$$\frac{\mathrm{d}\left(M_{\text{Maximum Projection Sphericity}}\right)}{\mathrm{d}\Delta_S} = \frac{(L^2+2Ld-2Lr_1+d^2-2dr_1+2r_1^2)^2}{12(L+d)(L+d-r_1)} \times \sqrt[3]{\frac{2}{r_1^5(2L+d)}} > 0 \quad (29)$$

Maximum Projection Sphericity exhibits a positive correlation with both volume and surface area asymmetry.

(5) Hayakawa Roundness (monitonicity: ambiguous)

(6) Spreading Index (monitonicity: ambiguous)

(7) Elongation Ratio (monotonicity: decreasing)

$$\frac{\mathrm{d}\left(M_{\text{Elongation Ratio}}\right)}{\mathrm{d}\Delta_V} = -\frac{(2L+d)[(L+d-r_1)^3+r_1^3]^2}{12r_1^4(L+d)(L+d-r_1)^2} < 0 \quad (30)$$

$$\frac{\mathrm{d}\left(M_{\text{Elongation Ratio}}\right)}{\mathrm{d}\Delta_S} = -\frac{(2L+d)(L^2+2Ld-2Lr_1+d^2-2dr_1+2r_1^2)^2}{8r_1^3(L+d)(L+d-r_1)} < 0 \quad (31)$$

Elongation Ratio exhibits a negative correlation with both volume and surface area asymmetry.

(8) Pivotability Index (monotonicity: uncorrelated)

$$\frac{\mathrm{d}\left(M_{\text{Pivotability Index}}\right)}{\mathrm{d}\Delta_V} = \frac{\mathrm{d}\left(M_{\text{Pivotability Index}}\right)}{\mathrm{d}\Delta_S} = 0 \quad (32)$$

Pivotability Index is not related to either volume or the asymmetry of surface area.

(9) Wilson Flatness Index (monotonicity: increasing)

$$\frac{\mathrm{d}(M_{\text{Wilson Flatness Index}})}{\mathrm{d}\Delta_V} = \frac{[(L+d-r_1)^3+r_1^3]^2}{3r_1^2(L+d)(2L+d)(L+d-r_1)^2} > 0 \quad (33)$$

$$\frac{\mathrm{d}(M_{\text{Wilson Flatness Index}})}{\mathrm{d}\Delta_S} = \frac{(L^2+2Ld-2Lr_1+d^2-2dr_1+2r_1^2)^2}{2r_1(L+d)(2L+d)(L+d-r_1)} > 0 \quad (34)$$

Wilson Flatness Index exhibits a positive correlation with both volume and surface area asymmetry.

(10) Hayakawa Flatness Ratio (monotonicity: decreasing)

$$\frac{\mathrm{d}\left(M_{\text{Hayakawa Flatness Ratio}}\right)}{\mathrm{d}\Delta_V} = -\frac{(2L+d)[(L+d-r_1)^3+r_1^3]^2}{24r_1^4(L+d)(L+d-r_1)^2} < 0 \tag{35}$$

$$\frac{\mathrm{d}\left(M_{\text{Hayakawa Flatness Ratio}}\right)}{\mathrm{d}\Delta_S} = -\frac{(2L+d)(L^2+2Ld-2Lr_1+d^2-2dr_1+2r_1^2)^2}{16r_1^3(L+d)(L+d-r_1)} < 0 \tag{36}$$

Hayakawa Flatness Ratio exhibits a negative correlation with both volume and surface area asymmetry.

(11) Huang Shape Factor (monotonicity: increasing)

$$\frac{\mathrm{d}\left(M_{\text{Huang Shape Factor}}\right)}{d\Delta_V} = \frac{[(L+d-r_1)^3+r_1^3]^2}{3r_1^2(L+d)(2L+d)(L+d-r_1)^2} > 0 \tag{37}$$

$$\frac{\mathrm{d}\left(M_{\text{Huang Shape Factor}}\right)}{\mathrm{d}\Delta_S} = \frac{(L^2+2Ld-2Lr_1+d^2-2dr_1+2r_1^2)^2}{2r_1(L+d)(2L+d)(L+d-r_1)} > 0 \tag{38}$$

Huang Shape Factor exhibits a positive correlation with both volume and surface area asymmetry.

(12) Corey Shape Factor (monotonicity: increasing)

$$\frac{\mathrm{d}\left(M_{\text{Corey Shape Factor}}\right)}{\mathrm{d}\Delta_V} = \frac{[(L+d-r_1)^3+r_1^3]^2}{12(L+d)(L+d-r_1)^2}\sqrt{\frac{2}{r_1^5(2L+d)}} > 0 \tag{39}$$

$$\frac{\mathrm{d}\left(M_{\text{Corey Shape Factor}}\right)}{\mathrm{d}\Delta_V} = \frac{(L^2+2Ld-2Lr_1+d^2-2dr_1+2r_1^2)^2}{8(L+d)(L+d-r_1)}\sqrt{\frac{2}{r_1^3(2L+d)}} > 0 \tag{40}$$

Corey Shape Factor exhibits a positive correlation with both volume and surface area asymmetry.

2. Cell Intercalation

During dorsal intercalation, the morphology of individual cells gradually elongates. We assume that the participating cells are composed of hemispherical ends connected by a cylindrical midsection. The radius of the hemispheres is denoted as r, and the height of the cylinder as H. Prior to intercalation, the cells display a perfect spherical shape with a radius of r; as the intercalation process progresses, they progressively assume an increasingly elongated capsule-like morphology. To analyzethe morphological dynamic, the fundamental parameters are calculated:

$$V = V_{\text{convex}} = \frac{4}{3}\pi r^3 + \pi r^2 H \tag{41}$$

$$S = S_{\text{convex}} = 4\pi r^2 + 2\pi r H \tag{42}$$

$$a = H + 2r \tag{43}$$

$$b = c = 2r \tag{44}$$

Then, substituting the formula given in Figure 1A [Guan et al., *Membranes*, 2024], the 12 morphology descriptors are presented by the following equation:

$$M_{\text{General Sphericity}} = \frac{\sqrt[3]{36\pi V^2}}{S} = \frac{1}{2(H+2r)}\sqrt[3]{4r(3H+4r)^2} \tag{45}$$

$$M_{\text{Diameter Sphericity}} = \frac{\sqrt[3]{\frac{6V}{\pi}}}{a} = \frac{1}{H+2r}\sqrt[3]{r^2(6H+8r)} \tag{46}$$

$$M_{\text{Intercept Sphericity}} = \sqrt[3]{\frac{bc}{a^2}} = \sqrt[3]{\left(\frac{2r}{H+2r}\right)^2} \tag{47}$$

$$M_{\text{Maximum Projection Sphericity}} = \sqrt[3]{\frac{c^2}{ab}} = \sqrt[3]{\frac{2r}{H+2r}} \tag{48}$$

$$M_{\text{Hayakawa Roundness}} = \frac{V}{S\sqrt[3]{abc}} = \frac{3H+4r}{12}\sqrt[3]{\frac{2r}{(H+2r)^4}} \tag{49}$$

$$M_{\text{Spreading Index}} = \frac{\sqrt[3]{36\pi V_{convex}^2}}{S_{convex}^2}\frac{1}{2(H+2r)}\sqrt[3]{4r(3H+4r)^2} \tag{50}$$

$$M_{\text{Elongation Ratio}} = \frac{a}{b} = 1 + \frac{H}{2r} \tag{51}$$

$$M_{\text{Pivotability Index}} = 1 \tag{52}$$

$$M_{\text{Wilson Flatness Index}} = \frac{c}{a} = \frac{2r}{H+2r} \tag{53}$$

$$M_{\text{Hayakawa Flatness Ratio}} = \frac{a+b}{2c} = \frac{H+4r}{4r} \tag{54}$$

$$M_{\text{Huang Shape Factor}} = \frac{b+c}{2a} = \frac{2r}{H+2r} \tag{55}$$

$$M_{\text{Corey Shape Factor}} = \frac{c}{\sqrt{ab}} = \sqrt{\frac{2r}{H+2r}} \tag{56}$$

We further validated whether morphological descriptos exhibit a consistent trend with the progression of dorsal intercalation (*i.e.*, as H increases and r decreases). Based on the total differential relationship:

$$\mathrm{d}M = \frac{\partial M}{\partial H}\mathrm{d}H + \frac{\partial M}{\partial r}\mathrm{d}r \tag{57}$$

Substituting specific morphology descriptors yields:

(1) General Sphericity

$$\mathrm{d}\left(M_{\text{General Sphericity}}\right) = -\frac{1}{2(H+2r)^2}\sqrt[3]{\frac{4r}{(3H+4r)}}\,\mathrm{d}H + \frac{H^2}{2(H+2r)^2}\sqrt[3]{\frac{4r}{r^2(3H+4r)}}\,\mathrm{d}r \tag{58}$$

General Sphericity decreases with increasing H and decreasing r.

(2) Diameter Sphericity

$$\mathrm{d}\left(M_{\text{Diameter Sphericity}}\right) = -\frac{4(H+r)}{(H+2r)^2}\sqrt[3]{\frac{r^2}{(6H+8r)^2}}\,\mathrm{d}H + \frac{4H(H+r)}{(H+2r)^2}\sqrt[3]{\frac{1}{r(6H+8r)^2}}\,\mathrm{d}r \tag{59}$$

Diameter Sphericity decreases with increasing H and decreasing r.

(3) Intercept Sphericity

$$\mathrm{d}\left(M_{\text{Intercept Sphericity}}\right) = -\frac{2}{3}\sqrt[3]{\frac{4r^2}{(H+2r)^5}}\,\mathrm{d}H + \frac{2H}{3}\sqrt[3]{\frac{4}{r(H+2r)^5}}\,\mathrm{d}r \tag{60}$$

Intercept Sphericity decreases with increasing H and decreasing r.

(4) Maximum Projection Sphericity

$$\mathrm{d}\left(M_{\text{Maximum Projection Sphericity}}\right) = -\frac{1}{3}\sqrt[3]{\frac{2r}{(H+2r)^4}}\,\mathrm{d}H + \frac{H}{3}\sqrt[3]{\frac{2}{r(H+2r)^4}}\,\mathrm{d}r \tag{61}$$

Maximum Projection Sphericity decreases with increasing H and decreasing r.

(5) Hayakawa Roundness

$$\mathrm{d}\left(M_{\text{Hayakawa Roundness}}\right) = \frac{2r-3H}{36}\sqrt[3]{\frac{2r}{(H+2r)^7}}\,\mathrm{d}H + \frac{H(3H-2r)}{36}\sqrt[3]{\frac{2}{r^2(H+2r)^7}}\,\mathrm{d}r \tag{62}$$

Hayakawa Roundness displays non-monotonicity, which increases with increasing H and decreasing r when $r > \frac{3}{2}H$, whereas it decreases with increasing H and decreasing r when $r > \frac{3}{2}H$.

(6) Spreading Index

$$\mathrm{d}\left(M_{\text{Spreading Index}}\right) = -\frac{1}{2(H+2r)^2}\sqrt[3]{\frac{4r}{(3H+4r)}}\,\mathrm{d}H + \frac{H^2}{2(H+2r)^2}\sqrt[3]{\frac{4r}{r^2(3H+4r)}}\,\mathrm{d}r \tag{63}$$

Spreading Index decreases with increasing H and decreasing r.

(7) Elongation Ratio

$$\mathrm{d}\left(M_{\text{Elongation Ratio}}\right) = \frac{1}{2r}\,\mathrm{d}H - \frac{H}{2r^2}\,\mathrm{d}r \tag{64}$$

Elongation Ratio increases with increasing H and decreasing r.

(8) Pivotability Index

$$\mathrm{d}\left(M_{\text{Pivotability Index}}\right) = 0 \cdot (\mathrm{d}H + \mathrm{d}r) \tag{65}$$

Pivotability Index is not related to the progress of dorsal intercalation.

(9) Wilson Flatness Index

$$\mathrm{d}\left(M_{\text{Wilson Flatness Index}}\right) = -\frac{2H}{(H+2r)^2}\,\mathrm{d}H + \frac{2h}{(H+2r)^2}\,\mathrm{d}r \tag{66}$$

Wilson Flatness Index decreases with increasing H and decreasing r.

(10) Hayakawa Flatness Ratio

$$\mathrm{d}\left(M_{\text{Hayakawa Flatness Ratio}}\right) = \frac{1}{4r}\mathrm{d}H - \frac{H}{4r^2}\mathrm{d}r \tag{67}$$

Hayakawa Flatness Ratio increase with increasing H and decreasing r.

(11) Huang Shape Factor

$$\mathrm{d}\left(M_{\text{Huang Shape Factor}}\right) = -\frac{2r}{(H+2r)^2}\mathrm{d}H + \frac{2H}{(h+2r)^2}\mathrm{d}r \tag{68}$$

Huang Shape Factor decreases with increasing H and decreasing r.

(12) Corey Shape Factor

$$\mathrm{d}\left(M_{\text{Corey Shape Factor}}\right) = -\frac{1}{2}\sqrt{\frac{2r}{(H+2r)^3}}\,\mathrm{d}H + \frac{H}{2}\sqrt{\frac{2r}{r(H+2r)^3}}\mathrm{d}r \tag{69}$$

Corey Shape Factor decreases with increasing H and decreasing r.

Based on the above mathematical derivation, the theoretical trend is highly consistent with the statistical trend of asymmetric division and dorsal intercalation presented in Figure 1E and 1F, Figure S2.

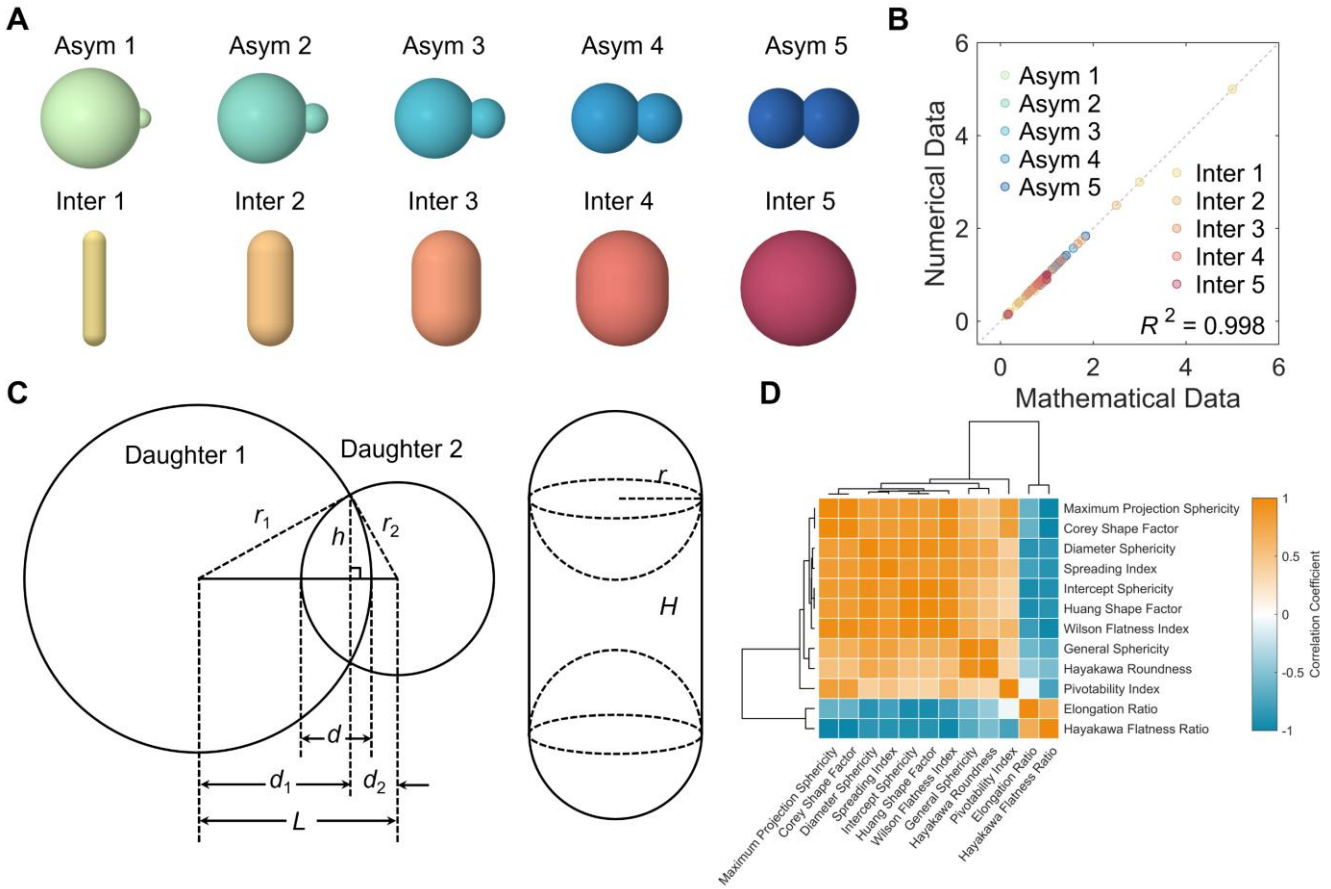

Figure S1. Mathematical and numerical analysis for cell morphology in cell division and cell intercalation.

(A) Mathematical models of dividing cells with varied division asymmetry (top) and intercalating cells with varied interaction depth (bottom), with details in METHOD DETAILS. (B) Consistency between the mathematical and numerical values of modeled morphologies of dividing cells with varied division asymmetry and intercalating cells with varied interaction depth. (C) Parameterized representation of modeled morphologies of dividing cells with varied division asymmetry and intercalating cells with varied interaction depth. (D) Clustering (based on agglomerative hierarchical clustering) of linear correlation coefficient (calculated with all cellular data in embryos under natural condition) among cell morphology descriptors.

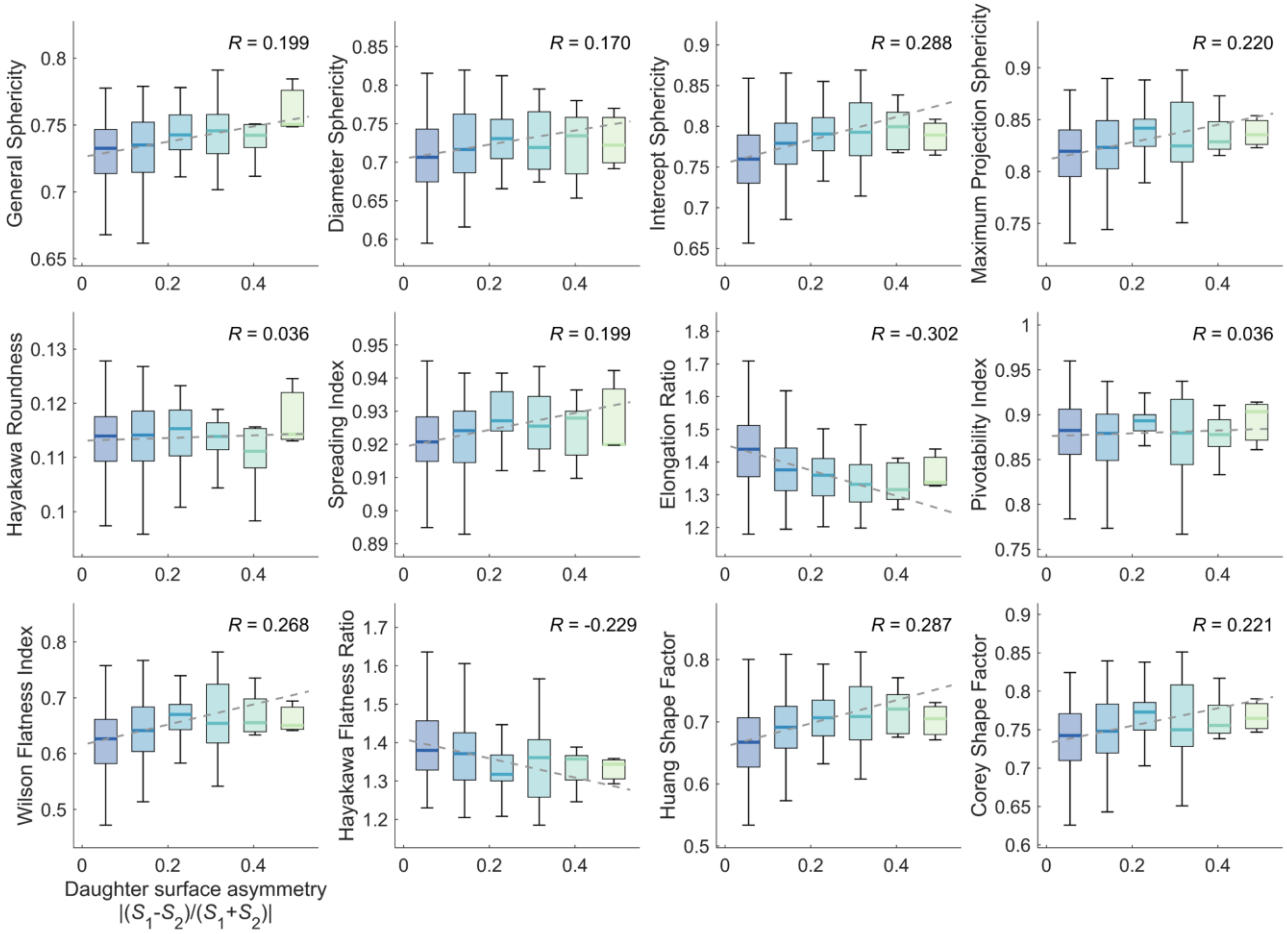

Figure S2. Change of cell morphology descriptors over daughter size asymmetry (daughter volume asymmetry), with the ones over daughter volume asymmetry in Figure 1E.

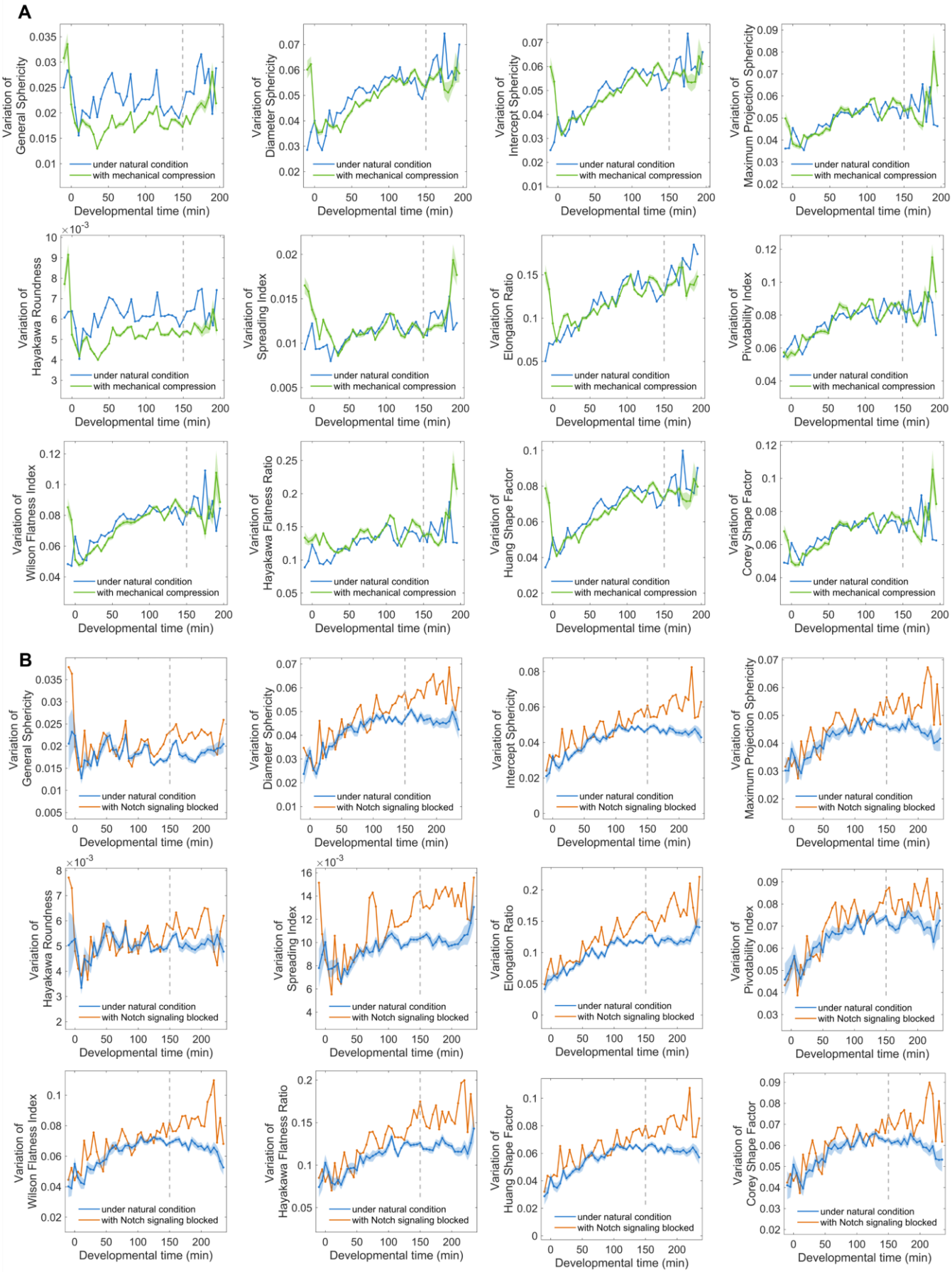

Figure S3. Cell morphology variation level (compared to the embryos under natural condition) in the embryos (A) with mechanical compression and (B) with Notch signaling blocked over developmental time (using the last moment of 4-cell stage as time zero), using all their individual embryo samples.

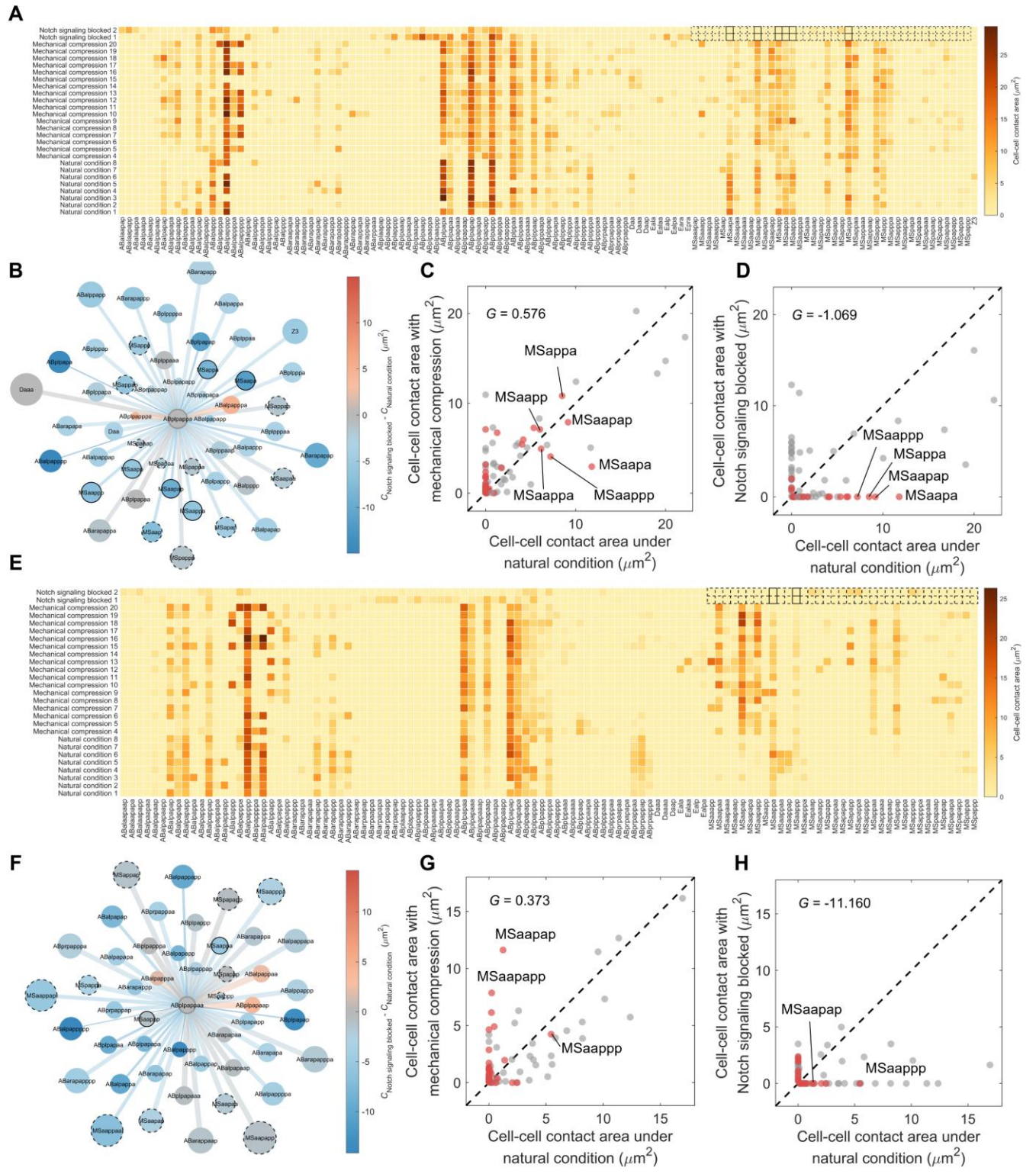

Figure S4. Cell morphology variation is well controlled during *C. elegans* embryonic development, remaining robustness with mechanical compression but not with Notch signaling blocked. (A) Cell-cell contact area in *C. elegans* embryos under natural condition (8 individual samples), with mechanical compression (17 individual samples), and with Notch signaling blocked (2 individual samples), centering the Notch signaling target and excretory cell progenitor ABplpappa, highlighting the previously reported Notch signaling (solid boundary) and non-signaling (dashed boundary) cells in MS lineage. (B) Change of cell-cell contact area, centering the Notch signaling target and excretory cell progenitor ABplpappa and highlighting the previously reported Notch signaling (solid boundary) and non-signaling (dashed boundary)

cells in MS lineage, where the circle area and band width are positively associated with cell volume and cell-cell contact area in embryos under natural condition. (C) Comparison of cell-cell contact area between embryos under natural condition and with mechanical compression, centering the Notch signaling target and excretory cell progenitor ABplpappa and highlighting the previously reported Notch signaling cells in MS lineage. (D) Comparison of cell-cell contact area between embryos under natural condition and with Notch signaling blocked, centering the Notch signaling target and excretory cell progenitor ABplpappa and highlighting the previously reported Notch signaling cells in MS lineage. (E) Cell-cell contact area in *C. elegans* embryos under natural condition (8 individual samples), with mechanical compression (17 individual samples), and with Notch signaling blocked (2 individual samples), centering the Notch signaling target and excretory cell progenitor ABplpappaa, highlighting the previously reported Notch signaling (solid boundary) and non-signaling (dashed boundary) cells in MS lineage. (F) Change of cell-cell contact area, centering the Notch signaling target and excretory cell progenitor ABplpappaa and highlighting the previously reported Notch signaling (solid boundary) and non-signaling (dashed boundary) cells in MS lineage, where the circle area and band width are positively associated with cell volume and cell-cell contact area in embryos under natural condition. (G) Comparison of cell-cell contact area between embryos under natural condition and with mechanical compression, centering the Notch signaling target and excretory cell progenitor ABplpappaa and highlighting the previously reported Notch signaling cells in MS lineage. (H) Comparison of cell-cell contact area between embryos under natural condition and with Notch signaling blocked, centering the Notch signaling target and excretory cell progenitor ABplpappaa and highlighting the previously reported Notch signaling cells in MS lineage.

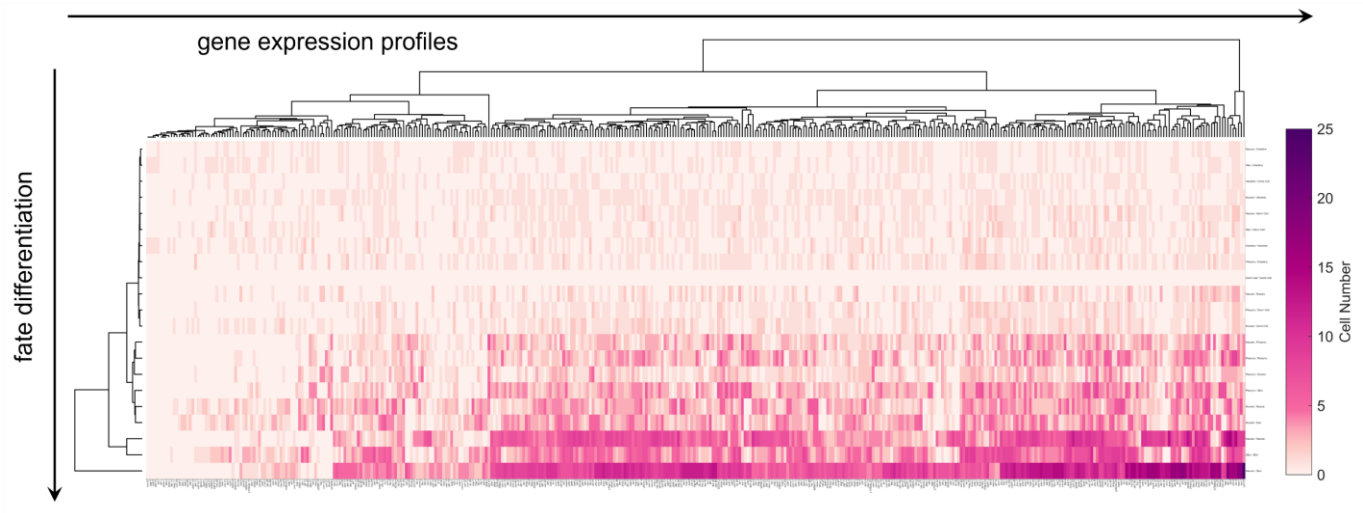

Figure S5. Clustering (based on agglomerative hierarchical clustering) of coupled differentiation events between cell fate pairs and gene expression profiles, illustrated in its complete mapping.

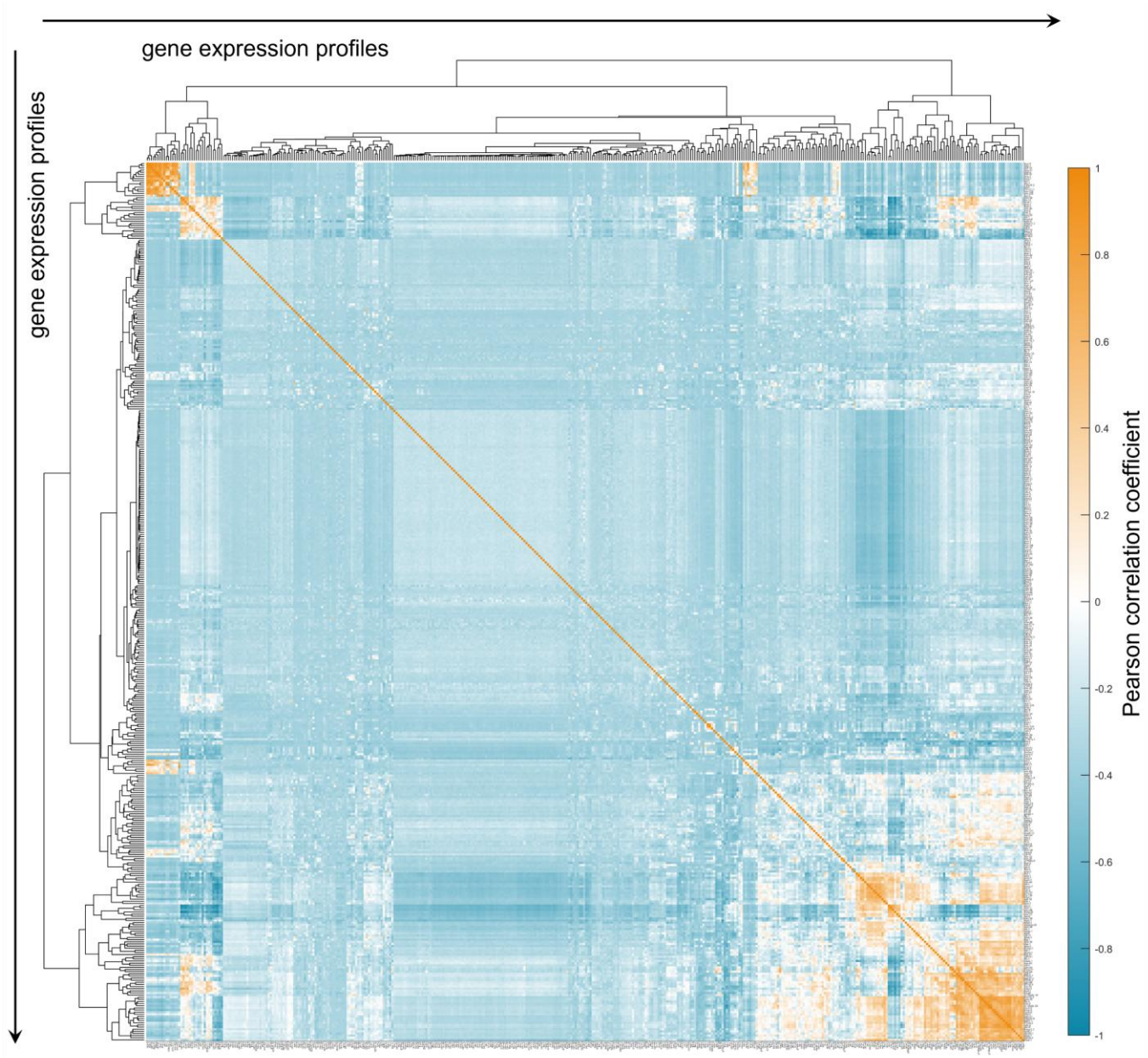

Figure S6. Clustering (based on agglomerative hierarchical clustering) of linear correlation coefficient among gene expression profiles.

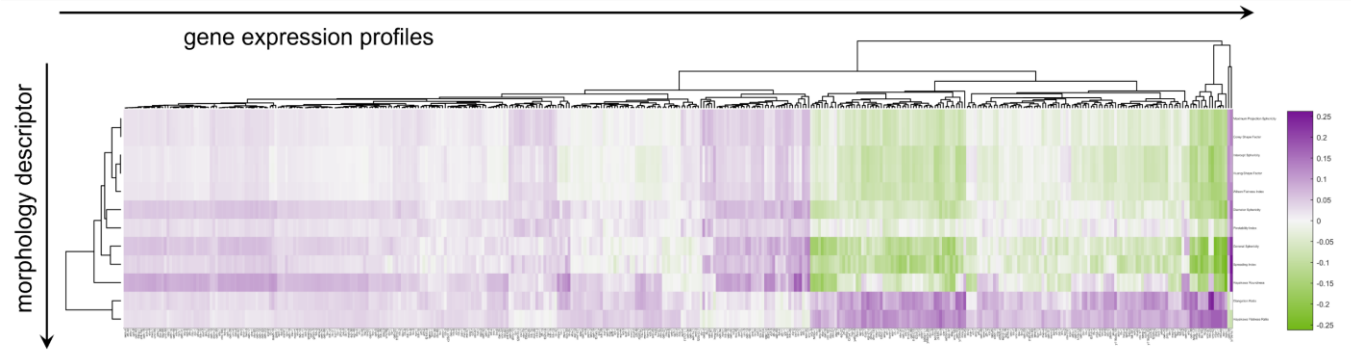

Figure S7. Clustering (based on agglomerative hierarchical clustering) of linear correlation coefficient between cell morphology descriptors and gene expression profiles.

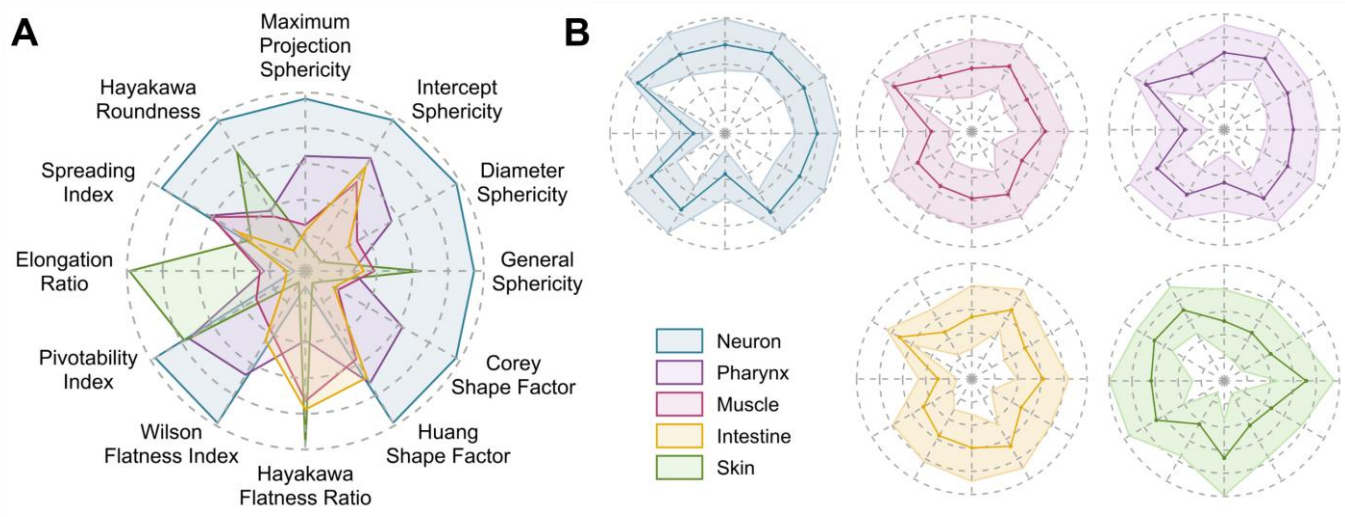

Figure S8. Radar diagram of morphology descriptors distinguishing neuron, pharynx, muscle, intestine, and skin, illustrated in their split distributions (mean ± standard deviation).

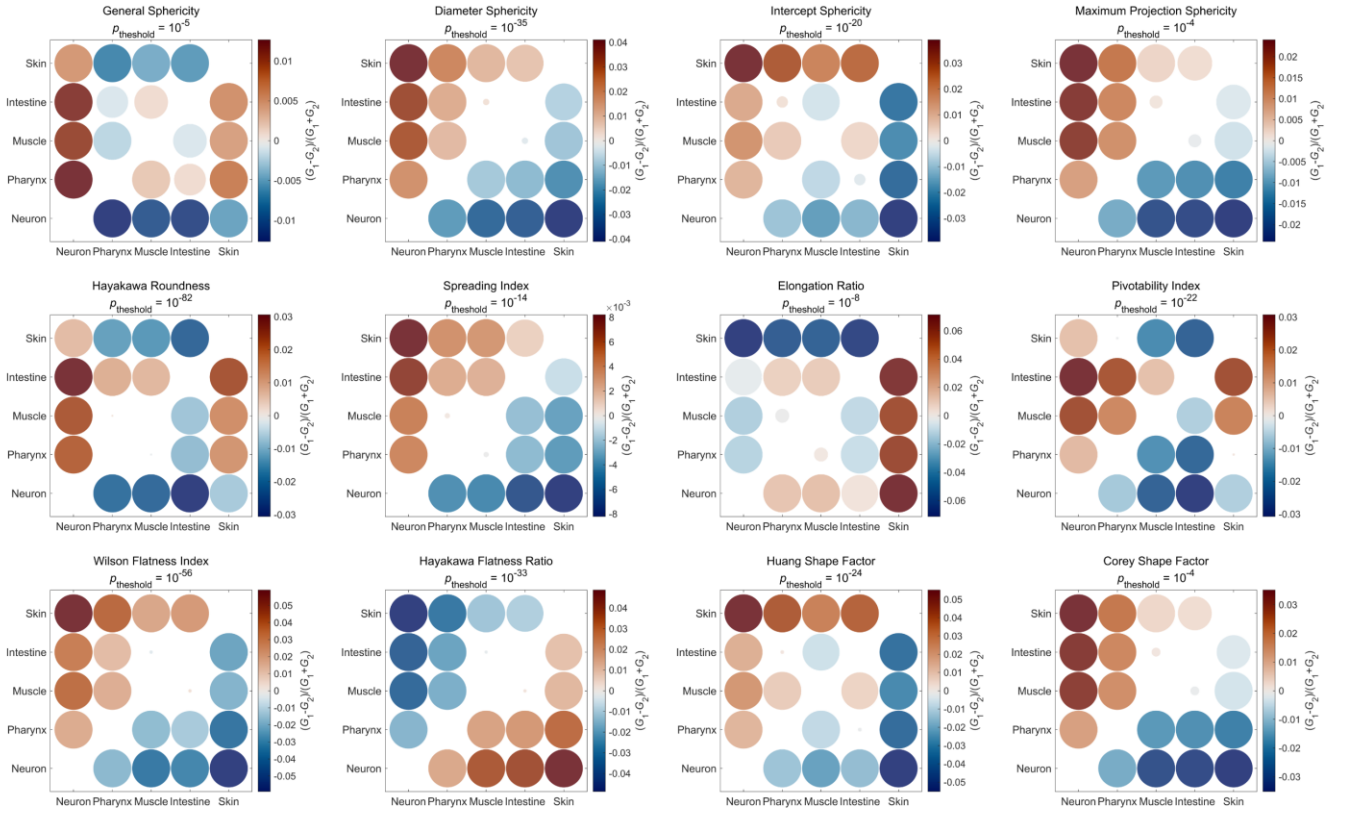

Figure S9. Distribution of asymmetry level (A_M) and statistical significance (p_M) in cell morphology differentiation distinguishing neuron, pharynx, muscle, intestine, and skin, shown by all morphology descriptors.

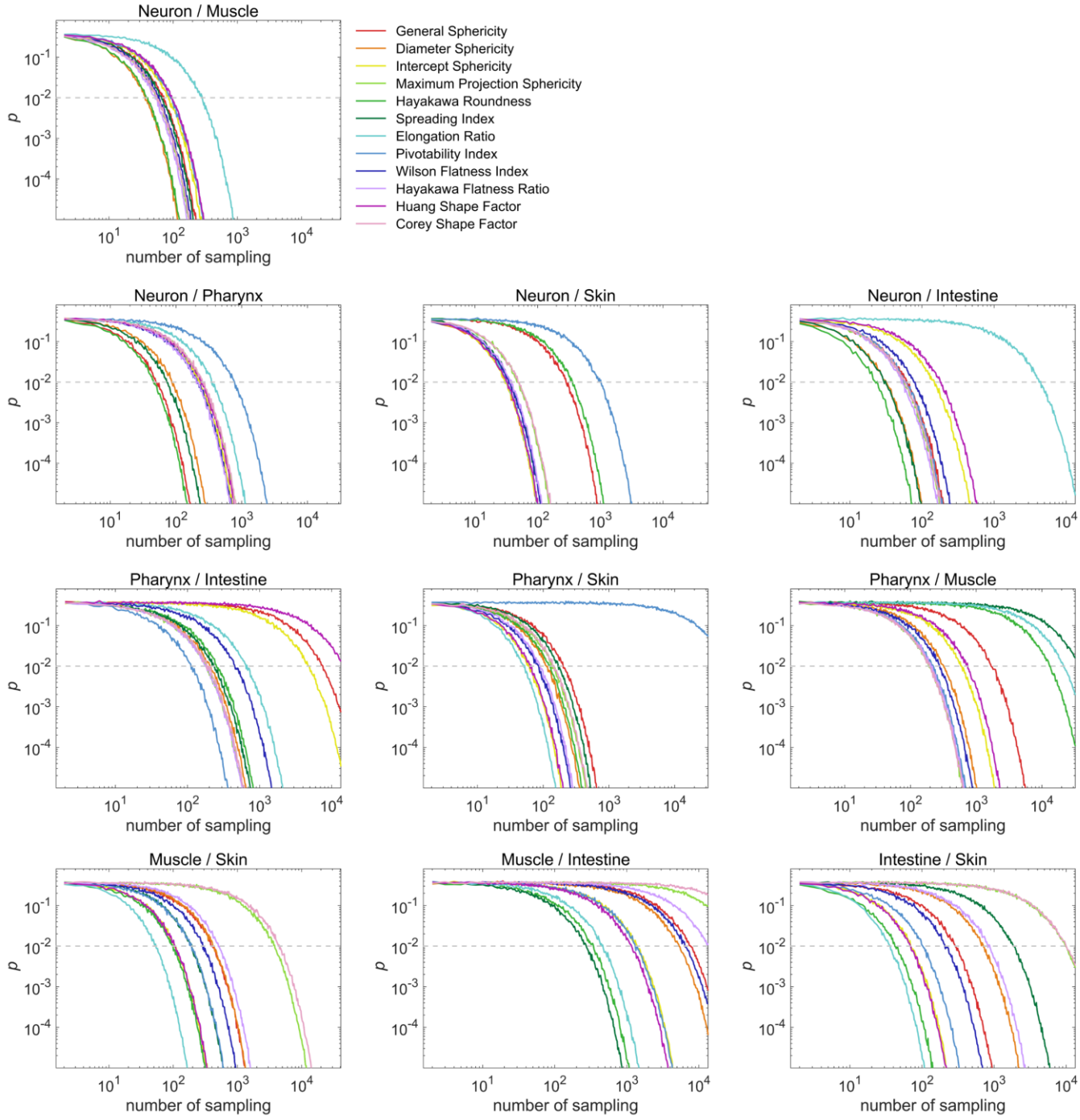

Figure S10. Change of statistical significance (p_{M}) over cell region sample size for predicting differentiation between cell fate pairs, shown by all 12 cell morphology descriptors with different sensitivity levels and all cell fate pairs.

SUPPLEMENTAL INFROMATION TITLES AND LEGENDS

FIGURE LEGENDS

Legends should be included in the submitted manuscript as a separate section. Each figure legend should have a brief title that describes the entire figure without citing specific panels, followed by a description of each panel. In writing the figure title, we encourage you to re-use the subheadings of the results section to make the relationship clear. For any figures presenting pooled data, the measures should be defined in the

figure legends (for example, "Data are represented as mean ± SEM."). Each legend should refer to any supporting items in the supplemental information (e.g., "See also Figure S1.").

TABLES

Please use the Microsoft Word table function to make tables; you may need to revise any tables that are not created using this function. Tables should include a title, and footnotes and/or legend should be concise. Include tables in the submitted manuscript as a separate section.

When creating tables, please adhere to the following guidelines:

- Do not submit tables in Excel or PDF format. Do not place an Excel table in a Word document.
- Format tables with Word's table function; do not use tabs or spaces to create a table.
- Tables should not include colored text or shading, but embedded graphics with color are OK.
- Do not use line breaks or spaces to separate data within a cell. Use separate cells for all discrete data elements within a table.
- Number distinct tables as Table 1, Table 2, Table 3, etc., rather than as Table 1a, Table 1b, Table 1c, etc.
- If bold or italic font is used within a table to indicate some feature of the data, please give an explanation of its usage in the legend.
- All abbreviations within a table must be defined in the table legend or footnotes.
- Footnotes should be listed with superscript lowercase letters, beginning with “a.” Footnotes may not be listed with numbers or symbols.